

Bundles of High-Refractive-Index Optical Fibers for THz-Imaging with Subwavelength Resolution (Review)

© D.G. Melikyants^{1,3}, V.N. Kurlov², K.I. Zaitsev¹, G.M. Katyba²

¹ Prokhorov Institute of General Physics, Russian Academy of Sciences, Moscow, Russia

² Osipyan Institute of Solid State Physics RAS, Chernogolovka, Russia

³ Bauman Moscow State Technical University, 105005 Moscow, Russia

e-mail: melikyants.d@yandex.ru

Received April 04, 2023

Revised April 07, 2023

Accepted April 14, 2023

Bunches or bundles of optical fibers find more and more applications in various fields of fiber optics, despite the relatively low resolution of such devices, which does not exceed the wavelength λ . One way to cope with this challenge is to use materials with a high refractive index, which will make it possible to achieve strong localization of radiation modes in the fiber. This review describes the use of sapphire fibers with a high refractive index $n > 3$ for these purposes. They are used as the basis for fiber bundles operating in the terahertz (THz) range and provide imaging with a spatial resolution that exceeds the Abbe diffraction limit for free space. Bundles of sapphire fibers of various configurations are fabricated, consisting of arrays of parallel and non-parallel fibers, and their spatial resolution is estimated theoretically and experimentally using both the analysis of the pair correlation function of disordered fiber packing and the THz-imaging. In particular, for a bundle consisting of parallel metal-coated fibers, the resolution varies along the aperture with an average value of 0.53λ , and in some areas it can achieve 0.3λ . In the case of tapered fiber bundle with dielectric coating the resolution is 0.35λ , which is much higher than the Abbe limit. The developed principles can be transferred to any spectral range where materials for fiber optics with a high refractive index are available. Finally, methods for reconstructing THz images of test binary objects obtained using the proposed bundles are described.

Keywords: optical fibers, sapphire, subwavelength spatial resolution, terahertz frequency range.

DOI: 10.61011/EOS.2023.06.56659.125-23

1. Introduction

In the context of rapid development of fiber optics, optical fiber bundles are attracting more and more interest in solving various problems of visualization and remote sensing [1–3]. Such arrays of fibers with a dielectric coating smaller than that of the fiber itself (or with a sputtered metal coating) have already found their application in endoscopic biomedical imaging [4–6], thermography [7], photoacoustics [8], fluorescent microscopy [9] and two-photon microscopy [10], Raman imaging [11], holography [12], low-coherence interferometry and depth-resolution imaging [13–15], etc. In addition, fiber bundles can be included in various equipment, including biomedical equipment [16–19]. The high demand for compatible small form factor optical systems suitable for high-resolution imaging and sensing stimulates further development of new technologies, materials, designs and image processing algorithms aimed at increasing spatial resolution [20] and reduction of image artifacts inherent in fiber bundles [21]. For example, maximum a-posteriori estimation, model-based reconstruction, and machine learning techniques have been recently applied to improve imaging performance using fiber bundles [22–24].

In most currently existing bundles, each fiber transmits radiation independently of the others, or with little cross-

exchange of radiation energy between neighboring fibers. Then the spatial resolution of the bundle is defined by the fiber packing period p , which cannot be less than the diameter d of an individual fiber. For materials with a low refractive index, the resolution of the fiber bundle is approximately equal to the wavelength of the transmitted radiation λ , further resolution improvement is impeded by the difficulty of retaining the energy of the transmitted mode in the core of the fibers, which have subwavelength size [20,25]. It is for this reason that traditional optical fiber bundles are not used for ultra-high resolution imaging [26].

As an alternative to imaging with a bundle of optical fibers, the use of a single multimode fiber can be considered [27]. The disadvantage of such systems is the need for time-consuming calculations when searching for exact solutions to incorrect inverse problems. Image reconstruction is also sensitive to intermodal beats and changes in fiber guiding properties because of bending.

Another method to achieve high spatial resolution is the use of so-called fiber-wire media [28–30], when dielectric fibers are replaced by metal wires. They are suspended in the free space between the object plane and the image plane and operate as independent plasmonic waveguides. Due to the strong localization of plasmonic modes near the

surface of metal wires, it is potentially possible to create an imaging system based on such fiber media with a resolution of up to $\sim 10^{-1}\lambda$ [28]. However, the additional losses that occur in the sheath of metal wires, scattering, and interwire energy exchanges reduce the efficiency of the fiber-wire media. These problems can be partially solved by placing an array of metal wires in a dielectric material, which acts as a protective sheath and minimizes the impact of the environment [31,32]. However, this approach significantly increases the absorption and scattering of plasmonic modes, thereby reducing the main attraction of using fiber media [33].

Recently, it has been proposed to use bundles of optical sapphire fibers to overcome the Abbe resolution limit in the THz range [25], due to the high refractive index of sapphire. Such fibers combine the unique physical properties of sapphire (in addition to the high refractive index, it features a low absorption coefficient, chemical inertness, mechanical and radiation resistance) with the technological advantages of growing crystals with the edge-define, film-fed growth (EFG) method, which allows the production of high quality flexible fibers directly from the Al_2O_3 melt without machining of crystals [34,35]. Theoretical and experimental studies of sapphire fiber bundles have confirmed their capabilities in subwavelength imaging [25] with low resolution, up to 0.3λ .

In addition, despite the increased resolution, the recording of the THz image read from the output facet of the fiber bundle (image plane) is a non-trivial task, which is actually a common problem for both optical fiber bundles and wire carriers. Indeed, bundles (or wire carriers) transmit near-field THz inhomogeneities from the object plane to the image plane, while image reading with a subwavelength resolution still requires a near-field imaging system with a scanning probe. This greatly limits the practical utility of such optical fiber assemblies and wire media. In order to solve this problem, it was proposed to use a tapered bundle of sapphire fibers with a high refractive index in the THz range [36]. Subwavelength diameter fibers are tightly stacked in the object plane (input plane of the bundle) for the near field sampling with subwavelength resolution. Then, the fibers diverge from the object plane and thus „stretch“ the captured near field, after which the field is read from the image plane using conventional diffraction-limited optics. Such a tapered fiber bundle was first studied numerically, and then fabricated and studied experimentally at a frequency of 0.33 THz. It has been confirmed that the fiber bundle has a resolution that exceeds the Abbe limit [36].

This review will discuss the prospects for using fiber bundles of various configurations to record THz images with subwavelength spatial resolution. First, bundles of parallel fibers are considered. In a bundle made up of metal-coated fibers, the resolution varies along the aperture with an average value of 0.53λ , and in some areas it can achieve 0.3λ . Second, a bundle is considered made up of tapered sapphire fibers with a dielectric coating, where the image is read using diffraction-limited optics and reaches an average of 0.35λ . The developed imaging principles will

make it possible to overcome the 0.5λ diffraction limit of spatial resolution with focusing in the free space and adapt almost any conventional diffraction-limited optics for near-field applications.

2. Bundle of parallel fibers

The section is organized as follows. First, information about the schematic diagram of the fiber bundle will be given and the resolution parameter δ will be calculated for several excited modes in a metal-coated fiber. Then, the process of fabricating parallel-laid fiber bundles of various configurations is shown. Then, the calculation of the experimental spatial resolution of a bundle of metal-coated optical fibers with an imperfect lattice is presented both on the basis of analysis of its pair correlation function and with direct measurement. Finally, an approach to the reconstruction of an image obtained using a bundle of parallel fibers with an imperfect lattice is described.

2.1. Schematic of the parallel fiber bundle and maximum spatial resolution estimate

To demonstrate high-refractive-index fiber bundles, the terahertz (THz) frequency range was considered, and crystalline sapphire was chosen as the material platform (the refractive index along the c axis is $n_0 > 3$ for the above-mentioned range). Fig. 1, *a, b* shows the schematics of fiber bundles with metal and dielectric environments.

Let us consider a bundle of fibers located at the nodes of an ideal close-packed hexagonal lattice, as shown in Fig. 1, *b*. Here d , T and p are the fiber diameter, the hexagonal lattice period, and the metal coating thickness, respectively. In the case of metal-coated fibers with a coating thickness much greater than the thickness of the skin layer at a given operating frequency, the radiation can be considered to be transmitted through each fiber independently without energy exchanges between neighbor fibers [1], and in the case of a dielectric coating this effect may be present.

It is known that for each mode that propagates in the fiber, there is a cutoff excitation frequency, i.e. this mode exists only at frequencies above the limiting one, which generally depends on the fiber diameter and the refractive index of the core. Let us write an expression for the wavelengths corresponding to the cutoff frequencies for the transverse magnetic ($\text{TM}_{m,n}$) and transverse electric ($\text{TE}_{m,n}$) modes in the core of a metal-coated dielectric fiber [1]:

$$\lambda_{m,n}^{\text{TM}} = \frac{\pi n_{\text{core}} d}{\gamma_{m,n}}, \quad \lambda_{m,n}^{\text{TE}} = \frac{\pi n_{\text{core}} d}{\psi_{m,n}}, \quad (1)$$

where n_{core} is refractive index of the fiber core, d is fiber diameter, $\gamma_{m,n} = 2.40, 3.83, 5.14, \dots$ and $\psi_{m,n} = 1.84, 3.05, 3.83, \dots$ are roots of the Bessel function of the 1st kind of order m and roots of its first derivative, respectively; $m, n = 0, 1, \dots, N$. Let us define the spatial resolution of the fiber bundle as the period T or the

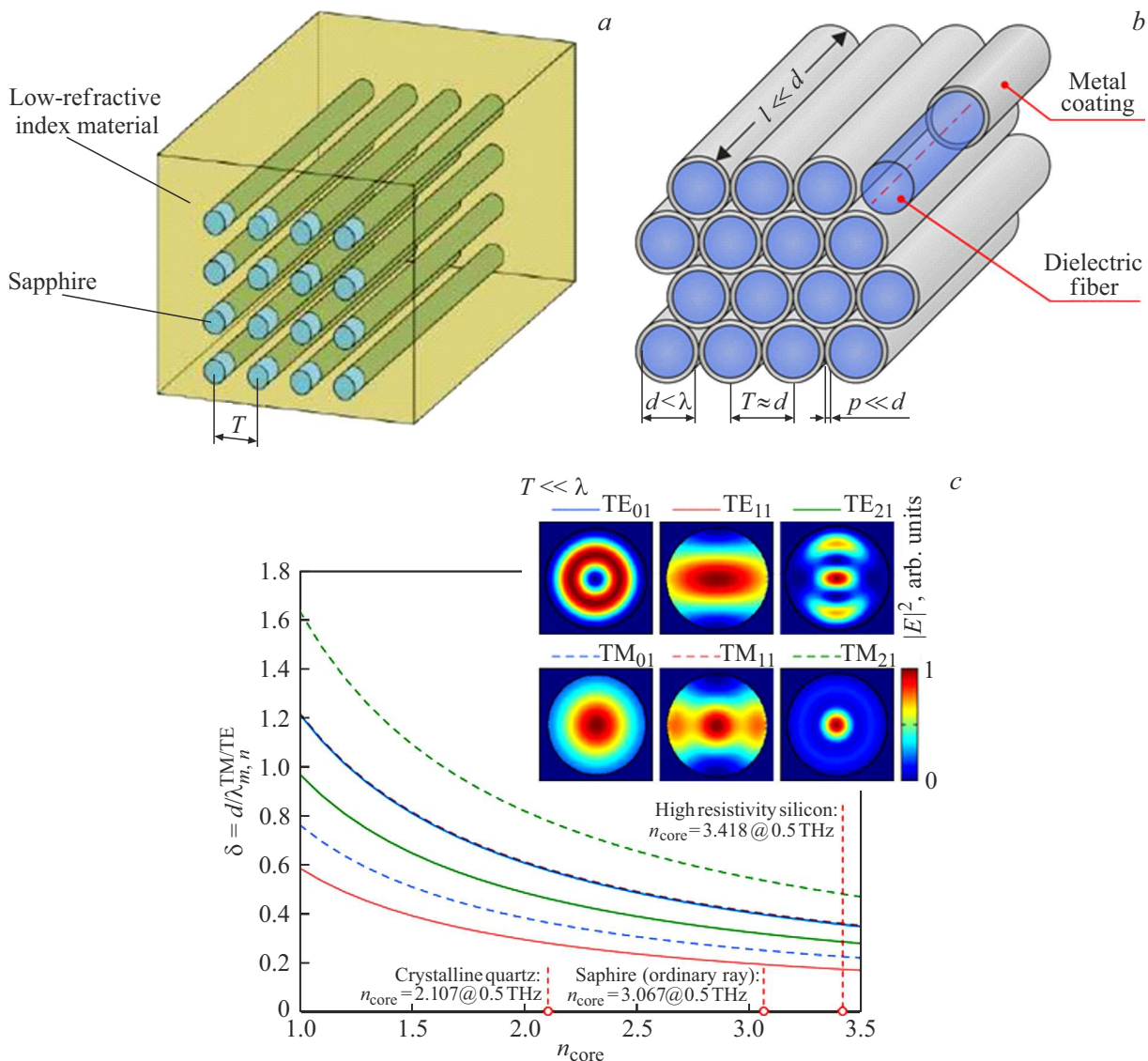


Figure 1. A bundle of dielectric fibers with a high refractive index and with a metal coating. (a) Schematic of the fiber bundle. (b) Theoretical estimation of the normalized bundle resolution δ as a function of the fiber core refractive index n_{core} for several lower order TM and TE fiber modes. Vertical dashed red lines in (b) correspond to the refractive indices of several common crystalline optical materials at a frequency of 0.5 THz [37]. Panels (b, c) are adapted from [25] with permission from Wiley publishing house.

diameter d (assuming $p \ll d$, therefore $T \approx d$), normalized to the operating wavelength λ . The maximum achievable spatial resolution δ is estimated as a function of n_{core} :

$$\delta_{\min} = \min_{m,n} \left[\frac{d}{\lambda_{m,n}^{TM}}, \frac{d}{\lambda_{m,n}^{TE}} \right] = \min_{m,n} \left[\frac{y_{m,n}}{\pi n_{core}}, \frac{\psi_{m,n}}{\pi n_{core}} \right] \approx \frac{1.84}{\pi n_{core}} \approx \frac{0.59}{n_{core}}, \quad (2)$$

it is minimal for the TE₁₁ mode. Due to the fact that this mode has an angular momentum of $m = 1$, it can be effectively excited with linearly polarized light, and thus with most THz field sources such as photoconductive antennas and backward wave tubes. Fig. 1, b shows the parameter δ as a function of n_{core} , calculated for several

low-order modes at their cutoff frequencies. Vertical dashed red lines show the refractive indices at 0.5 THz of three representative crystalline THz optical materials, namely crystalline quartz, sapphire, and high-resistivity float zone silicon (HRFZ-Si) [37]. Among them, sapphire and silicon have the highest refractive indices, however, only sapphire seems to be technologically suitable for use in fiber optics [38]. As n_{core} increases, the bundle resolution parameter δ decreases monotonically and achieves deep subwavelength values of ≈ 0.2 for the TE₁₁ mode, when $n_{core} > 3.0$. The corresponding intensity profiles of modes are shown in the panel inset (b).

The described approach to increasing the resolution of the fiber bundle is general and can be implemented for any region of the electromagnetic spectrum if materials

with a high refractive index are available [39]. Taking into account that the refractive index of most dielectric materials increases with increasing λ due to the contribution of various electric dipole excitations (which is determined by the Kramers-Kronig relations [40]), a conclusion can be made that the described concept is especially effective at low frequencies and in particular in the THz range [39].

In conclusion, it should be noted that the above analysis is also valid for bundles of optical fibers with a dielectric coating except for some modifications. In such fibers, the field does not become zero at the boundary but should remain a continuous function; in addition, the refractive index n_{cladd} of the sheath must be taken into account. Neglecting the radiation losses in sapphire, the following can be written [41]

$$\delta_{\min} = \frac{\gamma_{0,1}}{\pi \sqrt{n_{\text{core}}^2 - n_{\text{cladd}}^2}}, \quad (3)$$

where $\gamma_{0,1}$ are roots of the Bessel function of the 1st kind of the 1st order. However, in the case of such fiber bundles there is an energy exchange between neighbor fibers, which will also adversely affect the properties of such a dielectric fiber bundle.

2.2. Fabrication of the bundle of parallel sapphire fibers

Sapphire fibers are fabricated by the EFG growth technique using an automated system based on a weight sensor [42–44]. Using this growth method, it seems possible to produce sapphire-shaped crystals with a complex predefined cross-sectional geometry, as well as with a high quality of the surface and body of the crystal in the initial state. Such crystals make it possible to solve many complex problems in optics and photonics.

Fig. 2, *a* shows the schematic of the EFG setup for fabricating round sapphire fibers with a diameter of 175–325 μm , the length of the fabricated fibers can up to ≈ 50 cm. Basic elements of the setup are a 22 kHz induction-heated graphite susceptor and a molybdenum crucible. Growth was initiated by a single-crystal sapphire seed with the *c* axis directed along the growth direction, and Verneuil crystals were used as the starting material for melt formation. Sapphire fibers were grown from a thin film of Al_2O_3 melt formed on the top of a capillary die at a temperature of 2053°C, the growth chamber was filled with an inert gas (high-purity argon), the pressure was 1.1–1.3 atm. The pulling rate was about 50 mm/h. During the growth process, the Al_2O_3 melt was rising to the die through 0.25-mm-thick capillary channels. In general, the fibers are grown using the technique and equipment that was previously used for the one-step fabrication of hollow sapphire microstructured THz waveguides, as well as flexible sapphire fibers, which are described in detail in [42,45–48]. The main difference between these experiments and current studies is the use of a new molybdenum

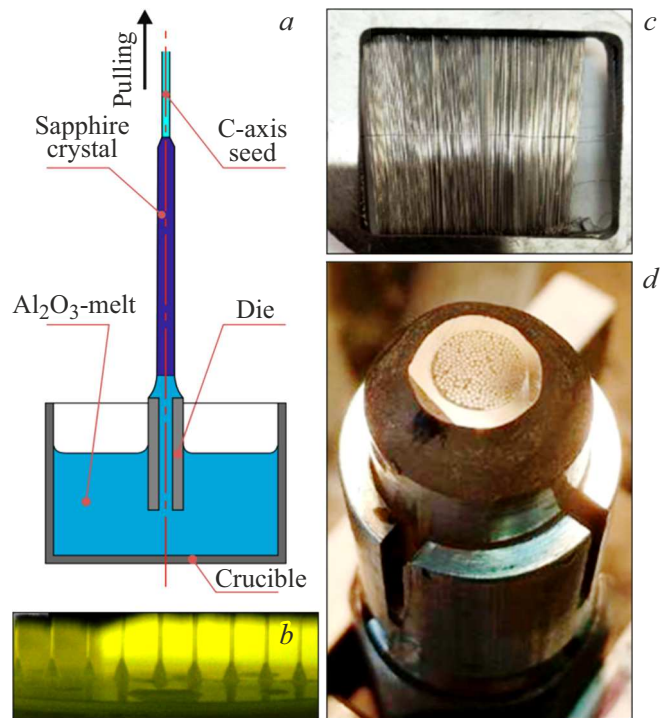


Figure 2. Fabrication of the metal-coated parallel sapphire fiber bundle. (a) Schematic of the sapphire fiber growth using the EFG-technique. (b) An *in situ* photo of the heating zone of the fiber growth in a multirun regime. (c) Photo of the sapphire fibers in a metal holder after vacuum sputtering of niobium (Nb) metal coating on their outer surface. (d) Photo of the fiber bundle, assembled inside a sapphire tube, fixed using epoxy, and mounted in a holder for grinding and polishing of the bundle end surfaces. The figure is adapted from [25] with permission from Wiley publishing house.

matrix (Fig. 2, *a*), as well as the possibility of growing fibers in a group mode (Fig. 2, *b*) [25], specially designed for the simultaneous fabrication of dozens of sapphire fibers in a single production cycle.

The grown sapphire fibers were cut into pieces and used to fabricate two types of parallel-laid bundles: metal-coated and dielectric-coated. Moreover, the metal-coated fibers were laid close to each other, and the dielectric fibers were laid with a certain period T exceeding the fiber diameter, in order to avoid energy exchange between neighbor fibers (the cross-talk effect).

The fibers intended for the fabrication of a bundle of sapphire fibers in a metal-coated dielectric matrix were placed in a metal holder for vacuum sputtering of a niobium (Nb) metal layer with a thickness of ≈ 300 nm (Fig. 2, *c*). The Nb coating was applied by vacuum sputtering using a Leubold-Heraeus Z-400 setup. In the process of sputtering, the holder with fibers was rotated to ensure a uniform coating thickness on the surface of the fibers. The sputtering was carried out in the atmosphere of high-purity argon at a pressure of $6 \cdot 10^{-3}$ mbar. The growth rate of the Nb film was ≈ 4 nm/s. When sputtered on a reference flat substrate

under equivalent conditions, the effective thickness of the Nb coating on the fibers was estimated as ≈ 300 nm.

After the metal was sputtered on the surface, the fibers were assembled into a bundle inside a hollow sapphire tube with an inner diameter of 6 mm; the bundle was impregnated with epoxy, which was then cured to increase the mechanical stability of the bundle (Fig. 2, *d*). Finally, the bundle was cut into pieces, which were then ground and polished on both sides. The resulting sample with a length of 20 mm is shown in Fig. 3 *b* together with a micrograph of one of the bundle facets.

The fabrication of a bundle of sapphire fibers of the second type included several stages. First, regular arrays of holes are formed in the metal foil, the diameter of each hole is slightly larger than the diameter of the fiber. The relatively large spacing between holes should ensure that the THz field is transmitted independently in each fiber and minimizes the energy exchange between neighbor fibers. Then, the sheets of metal foil with holes are fixed at a certain distance (approximately 2 cm). Then, sapphire fibers are introduced into the foil holes (in pilot experiments, fibers with a diameter of $300 \pm 25 \mu\text{m}$ were used); the fibers form a simple cubic lattice. The entire structure is impregnated with ED-20 epoxy resin with well-known optical properties in the THz range [49] with its subsequent curing. At the end, ends of the resulting structure are ground and polished and the metal foil is removed. A photo of a sample of the fabricated fiber bundle is shown in Fig. 3, *a*.

2.3. Experimental measurement of the optical properties of sapphire fiber bundles in the THz range

This section will present the results of studying the properties of a sapphire fiber bundle with a metal coating (the results of studying the properties of a fabricated sapphire fiber bundle with a dielectric coating will be presented in future studies).

2.3.1. Numerical simulation of the radiation propagation in a single metal-coated sapphire fiber.

The optical properties of the fabricated sapphire fiber bundles were studied numerically and experimentally in order to select the appropriate spectral operating range for THz imaging. To numerically analyze the propagation of radiation along a sapphire fiber, the finite-difference eigenmode method implemented in the Lumerical Mode Solutions software package was used [49]. Properties of a single sapphire fiber with a diameter of $300 \mu\text{m}$ surrounded by an ideal electrical conductor were simulated. The anisotropic THz optical properties of sapphire were taken from [25]. Fig. 4, *a* shows the effective refractive indices n_{eff} and propagation loss α (by power) for several low-order modes as function of frequency ν , where the color bar defines α in $[\text{dB cm}^{-1}]$. Assuming that the c axis of the crystal is directed along the fiber, the bulk THz optical properties of sapphire are taken from [37], taking

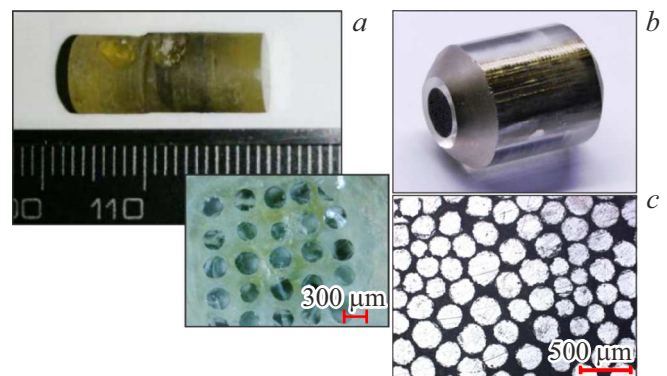


Figure 3. Bundles of parallel-laid sapphire fibers. (*a*) The pilot sample of the 2 cm-long bundle made on the basis of cylindrical sapphire fibers in a dielectric matrix, the fibers are arranged in a 5×5 (pixels) matrix, the distance between the fibers is about $450 \mu\text{m}$ (may differ due to the fact that the actually fabricated structure is somewhat disordered, see the inset). (*b, c*) An example of a metal-coated sapphire fiber bundle (the sample is 20 mm long) and a cross-sectional photo taken with an optical microscope. Panels (*b*) and (*c*) are adapted from [25] with permission from Wiley publishing house.

into account anisotropy, dispersion, and losses. It should be noted that the exact characterization of the properties of Nb coatings is a difficult task and is beyond the scope of this review. Indeed, as it has been discussed in [50,51], optical properties of metal films can differ significantly from those of bulk metal because they are sensitive to the method of metal film synthesis, as well as to the geometry of the film and substrate (important are factors such as film thickness, crystal domain size, film porosity, substrate type and orientation, etc. [50,52]). That is why, in our numerical calculations, we took the ideal boundary conditions of the electrical conductor as the surface of the films, which is not unusual for the THz range [33,53,54] and basically leads to an underestimation of the propagation loss in the fiber.

It can be seen in Fig. 4, *a* that there are several modes in a single sapphire fiber (TE_{01} , TE_{11} , TM_{11} , TE_{01}) in the frequency range of 0.45–0.95 THz with losses in the range of 2–9 dB cm^{-1} . As mentioned above, linearly polarized light can only excite modes with angular momentum $m = 1$, i.e. TE_{11} and TM_{11} . In addition, the loss for each mode increases significantly with increase in ν (due to the increase in the absorption of THz waves in bulk sapphire at higher frequencies) [37] and in the order of the mode. Due to the fact that all fibers in a bundle operate independently, we expect the fiber bundle as a whole to have optical properties similar to those of a single fiber.

2.3.2. THz pulsed spectroscopy of a bundle of sapphire fibers with metal sputtering.

To experimentally determine the THz optical characteristics of fiber bundles, a THz pulsed spectrometer (THz-TPS) was used, the measurements were carried out in the „transmission“ mode, which was previously used in [43]. The setup

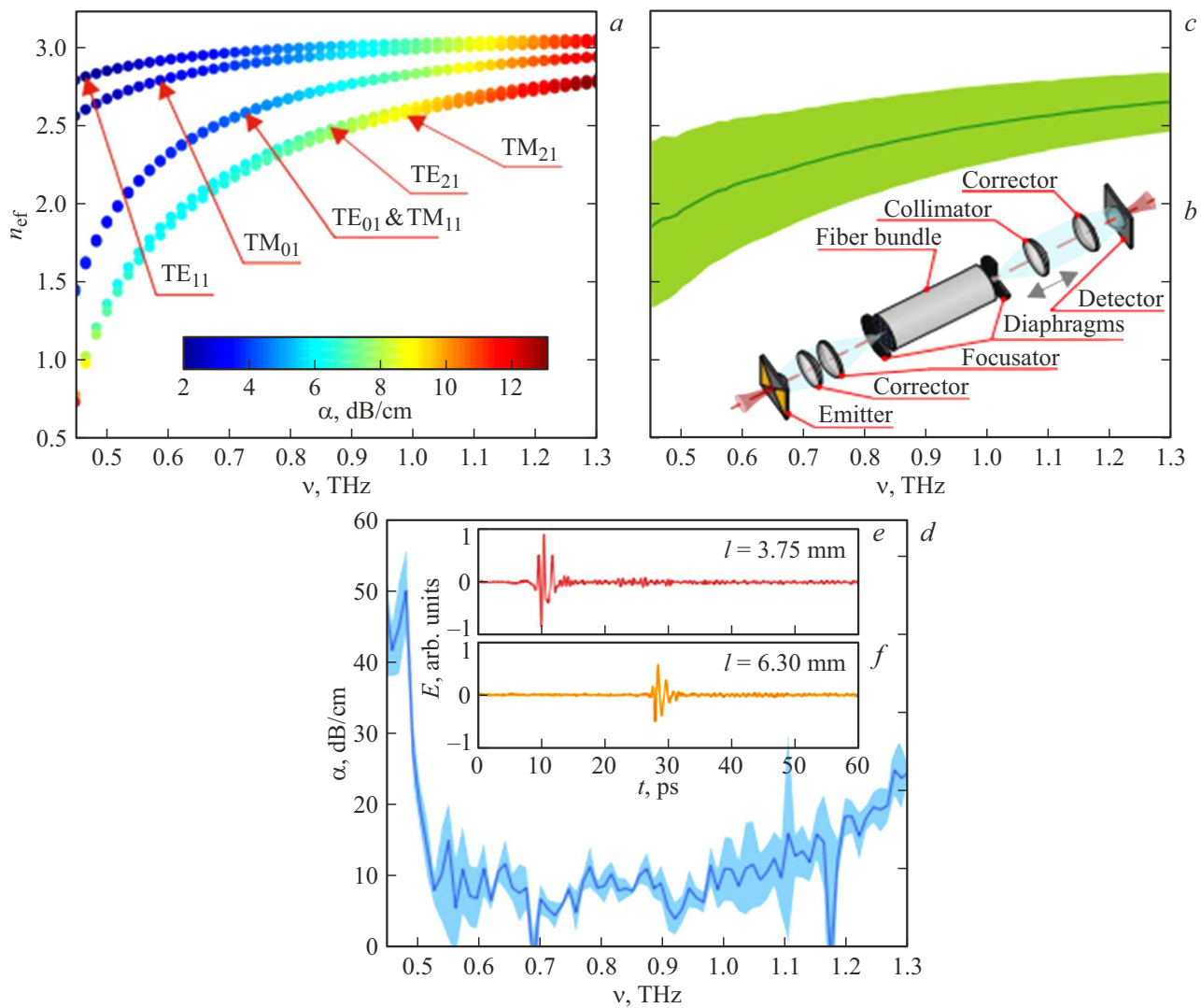


Figure 4. Numerical and experimental study of the waveguiding properties of a sapphire fiber bundle with metal sputtering. (a) FDE-calculated effective refractive index n_{eff} and propagation loss α (by power) as a function of the frequency ν for some lowest-order guided modes of a 300 μm -diameter sapphire fiber coated with a perfect electric conductor. (b) Schematic of the fiber bundle experimental characterization in a THz pulsed spectrometer. (c, d) Experimentally measured effective refractive index n_{eff} and loss α of the fiber bundle; (e, f) time-domain waveforms $E(t)$ of the THz pulsed spectrometer for the sapphire fiber bundle samples with lengths of $l = 3.75$ and 6.30 mm, respectively. The figure is adapted from [25] with permission from Wiley publishing house.

used photoconductive antennas made of LT-GaAs (BATOP GmbH) as a generator and detector of THz pulses. To excite nonequilibrium carriers in the antennas, a FemtoFerb 780 fiber laser (TOPTICA Photonics AG) was used that generated femtosecond laser pulses with a center wavelength of 0.786 μm , a duration of 93 fs, a pulse repetition rate of 98.59 MGz, and an average output power of 68.9 MW. The laser beam power was divided equally between the pump and the probe channels and was then attenuated in the optical path to provide the average 20 MW power in the arms of the spectrometer. Optical delay between the pump and probe pulses was varied using a double-pass linear mechanical delay stage (Zaber Technologies), with the positioning accuracy of $< 3 \mu\text{m}$ and the maximal travel distance of 101.6 mm. The generated THz radiation was

modulated at 10 kHz for further synchronous filtration. The pulse signal $E(t)$ was recorded with a 0.05 ps time-domain step. The duration of the recorded pulse was 100 ps, the resolution in the frequency domain was 10 GHz. The signal integration time was taken equal to 0.1 s, while no waveform averaging was used. During the measurement, the THz beam optical path was purged with the nitrogen gas to minimize the absorption of radiation by water vapor.

Fig. 4, b shows schematic of the part of the spectrometer with the waveguide under study. The emitted THz wave was collimated using a combination of the HRFZ-Si hemispherical lens (rigidly mounted onto the generating antenna) and the polymethylpentene (TPX) lens playing a role of corrector of spherical aberrations and mounted on a separate post; both lenses came from Batop GmbH.

The resultant collimated THz beam has a diameter of 25.4 mm. A single planoconvex TPX lens (focusator) with a focal length of 76.2 mm and a numerical aperture of $N_A = 0.16$ was used to focus the THz beam onto the input end of a fiber bundle through a diaphragm with a diameter of 5.5 mm. After propagating through the sample, the THz beam was collimated again by another TPX lens (collimator) with a focal length of 76.2 mm, and an identical diaphragm was fixed at the output end of the bundle. Finally, the beam was focused onto the antenna-detector using a corrector/hemispherical lens pair described above. The focusator was rigidly fixed, and the collimator was mounted on a rail and could be displaced to accommodate the fiber bundles of different lengths. As a result of the measurement, both the amplitude and the phase of the THz signal were recorded.

Due to the fact that the reconstruction of the effective refractive index and loss for various guiding modes of a fiber bundle is a difficult task [45], we used a different approach, in which the effective guiding properties of the bundle are determined, which can then be qualitatively compared with numerical data. For this purpose, two TPS waveforms $E_1(t)$ and $E_2(t)$ of fiber bundle pieces with two different lengths of $l_1 = 3.75$ mm and $l_2 = 6.30$ mm were measured. Based on these two waveforms, the effective refractive index n_{eff} and propagation loss α (by power) of the sapphire fiber bundle were reconstructed as follows. Consider the fundamental mode of an electromagnetic wave that propagates through a sample with a length l_2 :

$$\tilde{E}_{\text{large}}(\nu, l) = \exp\left(-i \frac{2\pi\nu}{c_0} \tilde{n}_{\text{eff}} l_2\right), \quad (4)$$

where \tilde{n}_{eff} is complex effective refractive index of the mode. Next, consider a plane wave $E_{\text{small}}(\nu, l)$, which propagates through an equivalent sample with a shorter length l_1 . The optical path lengths across the spectrometer cuvette for both waveguides can be expressed as follows:

$$l_{\text{opt},2} = \tilde{n}_{\text{eff}} l_2 + l_{\text{const}}, \quad (5)$$

$$l_{\text{opt},1} = \tilde{n}_{\text{eff}} l_1 + n_{\text{air}}(l_2 - l_1) + l_{\text{const}}, \quad (6)$$

where l_{const} defines a constant part of the THz beam path, which is the same for both samples. The ratio of the complex amplitudes of two frequency-domain signals can be written in the following form:

$$\begin{aligned} \frac{\tilde{E}_{\text{large}}(\nu)}{\tilde{E}_{\text{small}}(\nu)} &= \\ &= \frac{\exp\left(-i \frac{2\pi\nu}{c_0} n_{\text{Re}} l_2\right) \exp\left(-\frac{2\pi\nu}{c_0} n_{\text{Im}} l_2\right)}{\exp\left(-i \frac{2\pi\nu}{c_0} n_{\text{Re}} l_1\right) \exp\left(-\frac{2\pi\nu}{c_0} n_{\text{Im}} l_1\right) \exp\left(-i \frac{2\pi\nu}{c_0} (l_2 - l_1)\right)} \\ &= \left(-\frac{2\pi\nu}{c_0} n_{\text{Im}} (l_2 - l_1)\right) \exp\left(-i \frac{2\pi\nu}{c_0} (n_{\text{Re}} - 1)(l_2 - l_1)\right). \end{aligned} \quad (7)$$

Using this ratio of signals and assuming that the input-output losses are the same for the two bundles, their influence

can be eliminated. Thus, n_{eff} and the power attenuation coefficient α can be estimated as [46,55–57]:

$$n_{\text{eff}} = 1 + \frac{c_0}{2\pi\nu} \frac{1}{l_2 - l_1} \phi \left[\frac{F_t^{+1}[E_2]}{F_t^{+1}[E_1]} \right], \quad (8)$$

$$\alpha = \frac{-20}{l_2 - l_1} \lg \left| \frac{F_t^{+1}[E_2]}{F_t^{+1}[E_1]} \right|, \quad (9)$$

where $c_0 = 3 \cdot 10^8 \text{ m c}^{-1}$ is speed of light in the free space, $F_t^{+1}[\dots]$ is direct Fourier transform operator, $\phi[\dots]$ and $|\dots|$ are phase and modulus operators.

The reconstructed characteristics of fiber bundles together with time-domain signals are shown in Fig. 4, *c–f*. The errors in Fig. 4, *c, d* correspond to the confidence interval of measurements $\pm 1.5\sigma$, where σ is standard deviation. We believe, that the significant value of σ is related to the effects of intermodal beats (which is expected for low-mode and multimode transmission modes [45]), as well as to changes in the optical properties of the bundle at different points of the aperture. The measured effective refractive index is consistent with the predicted values n_{eff} corresponding to low order modes in individual metallized fibers. In turn, the measured propagation losses α are $\approx 10 \text{ dB cm}^{-1}$ in the frequency range of 0.45–1.0 THz, which is several times greater than those calculated numerically. The higher loss α is due to the finite conductivity of the thin Nb layer compared to the ideal electrical conductor used in the simulation. In addition to the expected increase in α at high frequencies due to the higher absorption of sapphire, losses increase rapidly at frequencies below 0.5 THz, and below 0.45 THz, the fiber bundle turns out to be almost opaque. Such a change in properties at lower frequencies may be due to the multimode character of the radiation transmission. Moreover, at frequencies below the fundamental cutoff frequency

$$\nu_{\text{cr}} \leq \frac{1.84c_0}{\pi n_{\text{core}}(d)} \quad (10)$$

stable modes may not exist in the bundle at all. For an average fiber diameter of $d = 250 \mu\text{m}$, the cutoff frequency is ≤ 0.2 THz. Considering that the diameters of the fibers in the fiber bundle are different (Fig. 3, *c*), it can be expected that some fibers of a smaller diameter will cease to conduct light at even higher frequencies.

In the case of a bundle made in this way, the operating frequency is chosen to be about 0.5 THz to maximize its resolution. This operating frequency is deliberately chosen close to the single-mode cutoff frequency of the sapphire fibers that make up the bundle. At such frequencies, the controlled mode is well localized inside the fiber core, and its partial overlap with a lossy metal coating still leads to controlled losses of $\approx 10 \text{ dB cm}^{-1}$.

At the same time, operation near the cutoff frequency leads to the smallest bundle resolution parameter δ due to the quasi-single-mode operation of the fibers that make up the pixels. More generally, due to the fact that the system we have developed is purely linear, the same concept

should be applied at higher frequencies with reduction of the size of the bundle and fibers. A practical challenge, however, is the reliable fabrication of the smaller diameter fibers required for the subwavelength imaging at frequencies above 1 THz. For example, subwavelength imaging at 2 THz requires sapphire fibers with a diameter of $\approx 50\text{--}75\ \mu\text{m}$ (to guarantee the single-mode transmission), which is beyond the capabilities of the EFG technique. In addition, today the most powerful yet quite affordable and compact THz sources operate at frequencies of $< 1\ \text{THz}$, and sources above 1 THz are usually low-power. Moreover, one of the key abilities of THz waves to penetrate objects that are opaque to the eye (such as most dry dielectrics) is mainly manifested at frequencies below 1 THz; at higher frequencies the material losses of dielectrics increase greatly. Therefore, applications for detection, imaging and security are often limited to the range below 1 THz.

2.3.3. Experimental determination of the spatial resolution of an imaging system based on a bundle of metal-coated parallel sapphire fibers. In this study, two different approaches to estimating the resolution of a fiber bundle are proposed, taking into account the non-ideal packing of fibers in a bundle. First, this is an analysis of the pair correlation function of the disordered fiber packing, and second, direct measurements using the „sharp blade“ method.

First, the disordered lattice formed by fiber center coordinates was analyzed. For this purpose, optical microscopy of facets of the fiber bundle was carried out (Fig. 5, *a* shows an optical image of one of the facets obtained with a microscope). By carrying out digital image processing, the coordinates of fiber centers in the cross section of the bundle were found. Then, Voronoi cells were calculated for the resulting real lattice of fibers (shown in Fig. 5, *b*, their color corresponds to the number of nearest neighbors). Fibers with 6 nearest neighbors correspond to well-structured bundle regions with an underlying hexagonal lattice. In contrast, regions with either more or fewer nearest neighbors correspond to an overpacked or underpacked lattice. The disordering of the fiber packing leads to a decrease in the spatial resolution because the hexagonal lattice is the most dense packing of cylindrical fibers. Using the obtained coordinates of nodes of a two-dimensional disordered lattice, the pair correlation function $g(\mathbf{r})$ was calculated [25]:

$$g(\mathbf{r}) = \frac{1}{m} \sum_j p_j(\mathbf{r} - \mathbf{r}_j), \quad (11)$$

where \mathbf{r} is vector in the bundle cross-section, $m = M/S$ is density of nodes (fiber centers) in the plane, M is number of nodes inside the region S , $p_j(\mathbf{r})$ is the probability density of locating a node in the position of the vector \mathbf{r} around the node j . In Fig. 5, *c* the pair correlation function calculated on the basis of experimental data is compared with the pair correlation function of an ideal hexagonal lattice. Due to the

fact that the resolution of a fiber bundle is determined by the distance between two nearest fibers, in a disordered lattice it can vary significantly across the aperture of the bundle. In this case, the possible values of the spatial resolution of the optical bundle should be characterized with the help of the probability density function calculated using the first peak of the pair correlation function (assuming that only the nearest neighbors contribute to the formation of this peak). It can be seen from Fig. 5, *c* that the first peak of the pair correlation function (and hence the bundle resolution) can be approximated using the Gaussian function:

$$p(\delta) = \frac{1}{\sqrt{2\pi}\sigma_\delta} \exp\left[-\frac{(\delta - \langle\delta\rangle)^2}{2\sigma_\delta^2}\right], \quad (12)$$

with the mean value of $\langle\delta\rangle = 0.53$ and the dispersion of $\sigma_\delta = 0.06$. Both parameters are normalized to the operating wavelength, which is taken equal to $\lambda = 600\ \mu\text{m}$ and corresponds to the lowest possible operating frequency of $\nu \approx 0.5\ \text{THz}$, as discussed in the previous section.

The proposed approach to estimating the resolution of a fiber bundle is quite general and can be used for any disordered fiber bundle, regardless of its operating frequency [2–19], as well as for analyzing various fiber media [28–32]. Thus, using only geometric data for a lattice composed of fiber centers, the spatial resolution of the bundle can be predicted, assuming that there is no energy exchange between individual fibers.

The characterization of the spatial resolution of the bundle was also carried out by conducting the so-called „sharp blade“ test. For this purpose, test opaque objects with sharp edges (semi-infinite plane) were visualized at a wavelength of $\lambda = 600$ (a frequency of $\nu \approx 0.5\ \text{THz}$), the transmission of which can be defined by a Heaviside step function. Then, the point spread function (PSF) of the imaging system and, accordingly, its spatial resolution are determined. The object is a strip of metal foil with a straight edge. A backward wave tube (BWT) was used as a source of continuous THz radiation, the spectral linewidth was $10^{-5}\nu$, the power was $10^{-2}\ \text{W}$. A Golay cell [34] was used as a beam intensity detector, which has a sensitivity of $10^{-5}\ \text{V/W}$ and a time constant of 0.1 s. A 22 Hz mechanical chopper was applied in order to modulate the THz beam intensity, which was further demodulated by a detector.

The measurement scheme is shown in Fig. 5, *d*, and the foil image in the THz range is shown in Fig. 5, *f*. The THz image contains distortions caused by the disorder of the bundle structure, as well as variations in the transmission of the bundle over its aperture.

In the experimental setup, the displayed object is located at a small distance (less than λ) in front of the input facet of the bundle and is illuminated by a slightly focused spatially homogeneous beam of THz radiation. With such a small distance between the object and the bundle, the geometric „shadow approximation“ is valid, according to which the distribution of radiation in the object plane is equal to the distribution in the plane of the input facet of

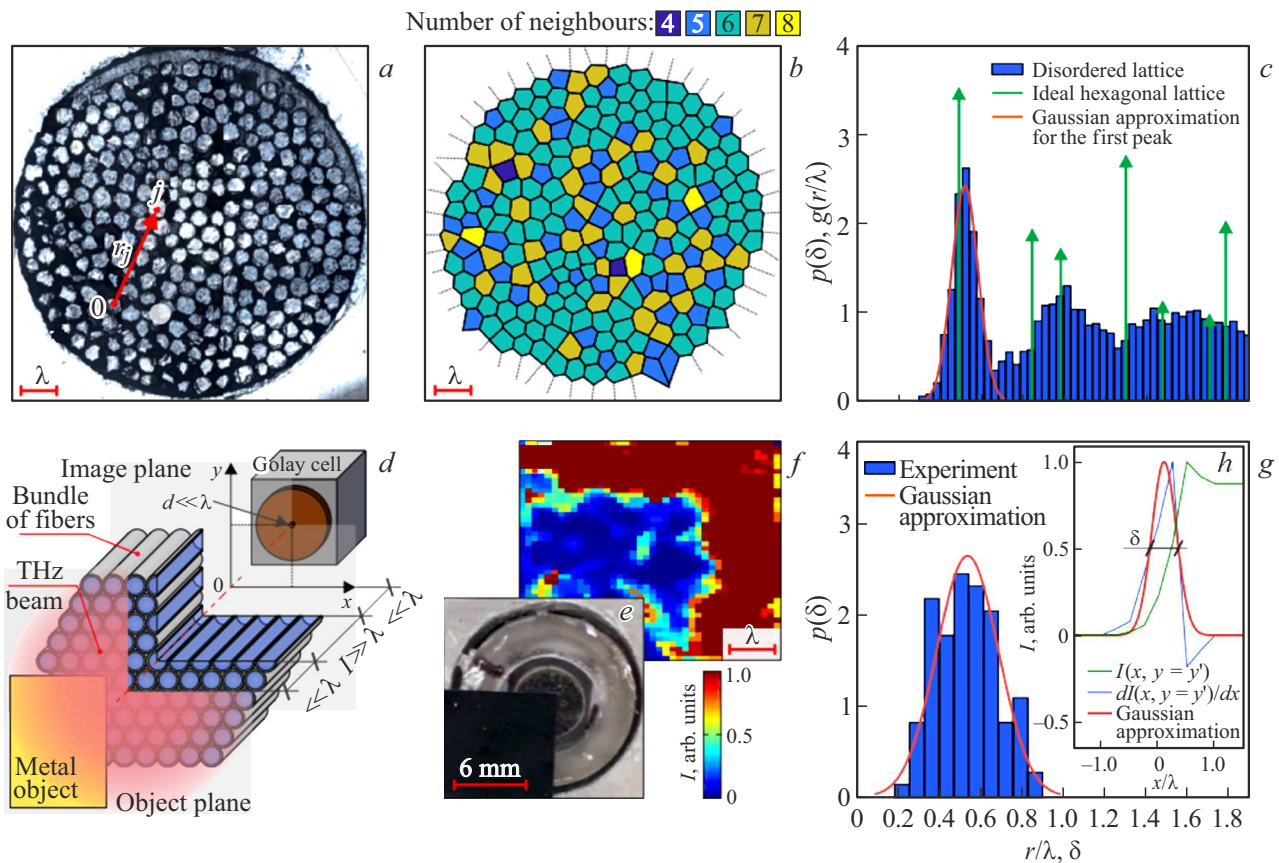


Figure 5. Experimental determination of the spatial resolution of the fabricated sapphire fiber bundle with THz imaging at a wavelength of $\lambda = 600 \mu\text{m}$. (a) Photo of a bundle facet taken with an optical microscope, where \mathbf{r}_j defines the spatial coordinates of the j -th fiber center (node). (b) Voronoi cells for the corresponding disordered 2D lattice formed by sapphire fibers; the cells are colored according to the number of nearest neighbors of each node. (c) Pair correlation function $g(\mathbf{r})$ for the ideal hexagonal (green) and disordered (blue) fiber lattices. The first peak can be used to characterize resolution variation across the bundle aperture, it is approximated by the Gaussian function (red curve). (d) Schematic of the THz-imaging using fiber bundles. (e, f) Optical image of the metal corner object placed in contact with the bundle input facet, and the corresponding THz image of the object read by the scanning diaphragm at the bundle output facet. (g) Probability density $p(\delta)$ for the resolution parameter distribution δ in independent measurements, obtained by statistical analysis of THz images. (h) The process of estimating the resolution parameter δ at a given point of the bundle aperture. Green color — intensity profile along a line in the THz image near the object edge $I(x, y = y_0)$; blue color — its first derivative $dI(x, y = y_0)/dx$, FWHM of the derivative peak defines the local resolution parameter δ . The figure is adapted from [25] with permission from Wiley publishing house.

the bundle. This allows us to treat the input facet of the bundle as an object plane. The radiation not blocked by a metal test object was introduced into the bundle and read from its output surface using a scanning diaphragm with a diameter of $200 \mu\text{m}$, which was also located near the image plane. The scattered THz field on the shadow side of the subwavelength diaphragm was recorded using a Golay cell. Both the diaphragm and the Golay cell were installed on a 2D motorized translation stage, which yields raster-scan of the image plane with the positioning accuracy of $< 2 \mu\text{m}$.

Fig. 5, g–h shows the results of the resolution estimation. Insert (h) illustrates the resolution estimation process for a specific position in the bundle aperture. Thus, for a fixed vertical position y_0 , consider the intensity profile $I(x, y = y_0)$ in the horizontal direction x on a THz image that contains a sharp change in intensity due to the foil angle. The derivative $dI(x, y = y_0)/dx$ has a sharp peak

for the coordinate x corresponding to the „foil-free space“ transition, and will simultaneously be the scattering function of the above-mentioned imaging system [58]. The same is true for the derivative of the intensity profile in the vertical direction $I(x = x_0, y)$. To characterize the spatial resolution δ at a specific point, we use the full width of half-maximum (FWHM) of the intensity derivative peak. It is worth noting that the resolution parameter δ was measured in different areas of the fiber bundle aperture (along the vertical and horizontal sides of the test object in y and x directions (Fig. 5, f) by independent measurements. Thus, the statistical distribution $p(\delta)$, which determines fluctuations in the resolution of the bundle over its aperture, is found and approximated by the Gaussian function (equation (12)); the results are shown in Fig. 5, g.

A direct experimental sample of the bundle resolution shows the mean value of $\langle \delta \rangle = 0.53$ and the standard

deviation of $\sigma_\delta = 0.15$; both parameters are normalized to the operating wavelength. It is noteworthy that the average resolution (δ) correlates very well with the data obtained by analyzing the pair correlation function and presented earlier. At the same time, the direct sampling method predicts a significant change in the resolution over the entire aperture of the bundle (the dispersion σ_δ is 2.5 times higher than that resulted from the analysis of the pair correlation function). The increase in σ_δ (with direct measurement of δ) can be caused by several factors that are not taken into account when performing the pair correlation function analysis. For example, imperfect cleavage of fiber ends that occur when grinding and polishing the facets of the bundle (Fig. 3, *b* and 5, *a*) can lead to significant scattering of THz radiation when it is input and output to/from the bundle, as well as to re-reflections of radiation inside the bundle. Fluctuations in the diameter and ellipticity of sapphire fibers along the entire length of the bundle, as well as microbends inside it, can result in the excitation of higher-order modes with highly asymmetric fields. Finally, incomplete congruence between the fiber coordinates at the object and image planes can result in skewed images.

The abovementioned imperfections can result in significant variation of the individual fiber transmission over the bundle aperture, which, in turn, can affect the resolution of the imaging system. A more detailed analysis of the detrimental impact of these factors on the sapphire fiber bundle performance, as well as search for the ways to minimize their effect will be the goals of our future activities.

Overall, both the pair correlation function analysis and the THz imaging of the opaque metal corner reveal strong potential for the subwavelength THz imaging using fabricated sapphire fiber bundles. Even the presented structure with non-optimal fiber packing shows the average resolution of (δ) = 0.53 with the lowest resolution reaching $\delta = 0.3$ at certain positions of the bundle. Such resolutions overcome the Abbe diffraction limit (0.62λ) of the conventional free-space imaging systems, and thus the structure under consideration has a great potential for subwavelength THz microscopy.

2.3.4. Reconstruction of images obtained using a bundle of parallel-laid metal-coated sapphire fibers. Imaging using fiber bundles typically suffers from various image distortions, among which, of particular importance are inhomogeneities in the THz-image intensity due to fluctuations of the individual fiber transmissions over the bundle aperture. A direct approach to mitigate this distortion type is to perform image normalization by the reference one (the image of the bundle in the absence of an object). Particularly, the normalized image $I_n(\mathbf{r})$ is computed based on the sample signal $I_{\text{raw}}(\mathbf{r})$ and the reference signal $I_{\text{ref}}(\mathbf{r})$ using the following regularization

procedure:

$$I_n(\mathbf{r}) = \frac{I_{\text{raw}}(\mathbf{r})}{I_{\text{ref}}(\mathbf{r})} \left(1 + \kappa \frac{N}{I_{\text{ref}}(\mathbf{r})} \right)^{-1}, \quad (13)$$

where $N = 0.095\%$ corresponds to the noise level at $I_{\text{raw}}(\mathbf{r})$ and $I_{\text{ref}}(\mathbf{r})$, $\kappa = 10^{-3}$ is an empirically determined regularization parameter [35] (we assume that N and κ are constant over the entire image plane). In Equation (13), the first ratio defines a simple inverse filtering and yields properly corrected image intensity, while the second term turns into 1 when $I_{\text{ref}}(\mathbf{r}) \gg N$, or into 0 when $I_{\text{ref}}(\mathbf{r}) \ll N$, and serves to mitigate the noise inherent to the simple inverse filtering [35].

Fig. 6 illustrates an example of the procedure for obtaining a THz image of a test binary object. The object of control is a metal grating (Fig. 6, *a*) with a period of 1.8 mm and a metal strip width of 0.9 mm, made of thick ($\ll \lambda$) aluminum foil. Fig. 6, *c* shows the raw image $I_{\text{raw}}(\mathbf{r})$ obtained using the bundle. The reference image $I_{\text{ref}}(\mathbf{r})$ is shown in Fig. 6, *b* and was obtained with the same bundle without grating. Finally, the normalized image $I_n(\mathbf{r})$ obtained using the regularization procedure (13) is shown in Fig. 6, *d*. Although the image quality enhancement using the simple inverse filtering is visibly clear, further image improvement is possible using more advanced techniques, such as Wiener inverse filter and alternative regularization procedures [35] or other methods, such as machine learning and model-based image reconstruction [21–23].

It is worth to note that no specific pixelization noise is observed in the image, which is usually inherent in imaging through optical fiber. This is due to the scanning-diaphragm-based THz image readout, used in our study, because such readout techniques automatically lead to image smoothing due to the small distance between sapphire fibers in a bundle and large sizes of the fiber cores.

Along with simplicity, the considered type of an image readout allows avoiding distortions to the THz-image by minimizing wave diffraction at the output end of the fiber bundle. Indeed, the geometric „shadow approximation“ [36] is valid for describing the near-field transfer from the bundle output facet to the scanning diaphragm, because the axial distance between them is $\ll \lambda$. In addition, when using subwavelength diaphragm image readout and a coherent radiation source, the distance between the output facet of the bundle and the diaphragm can be increased to $\sim \lambda$, and the image distortion due to diffraction can be numerically compensated by solving the integral equations of the vector diffraction theory as demonstrated, for example, in [41]. At the same time, the scanning aperture type of the THz-image readout is time-consuming and suffers from low energy efficiency. Particularly, this difficulty can be mitigated using bundles of tapered fibers featuring over the diffraction limit mode sizes at their output ends (Sec. 3).

While the presented example shows strong potential of high-refractive-index fiber bundles for subwavelength

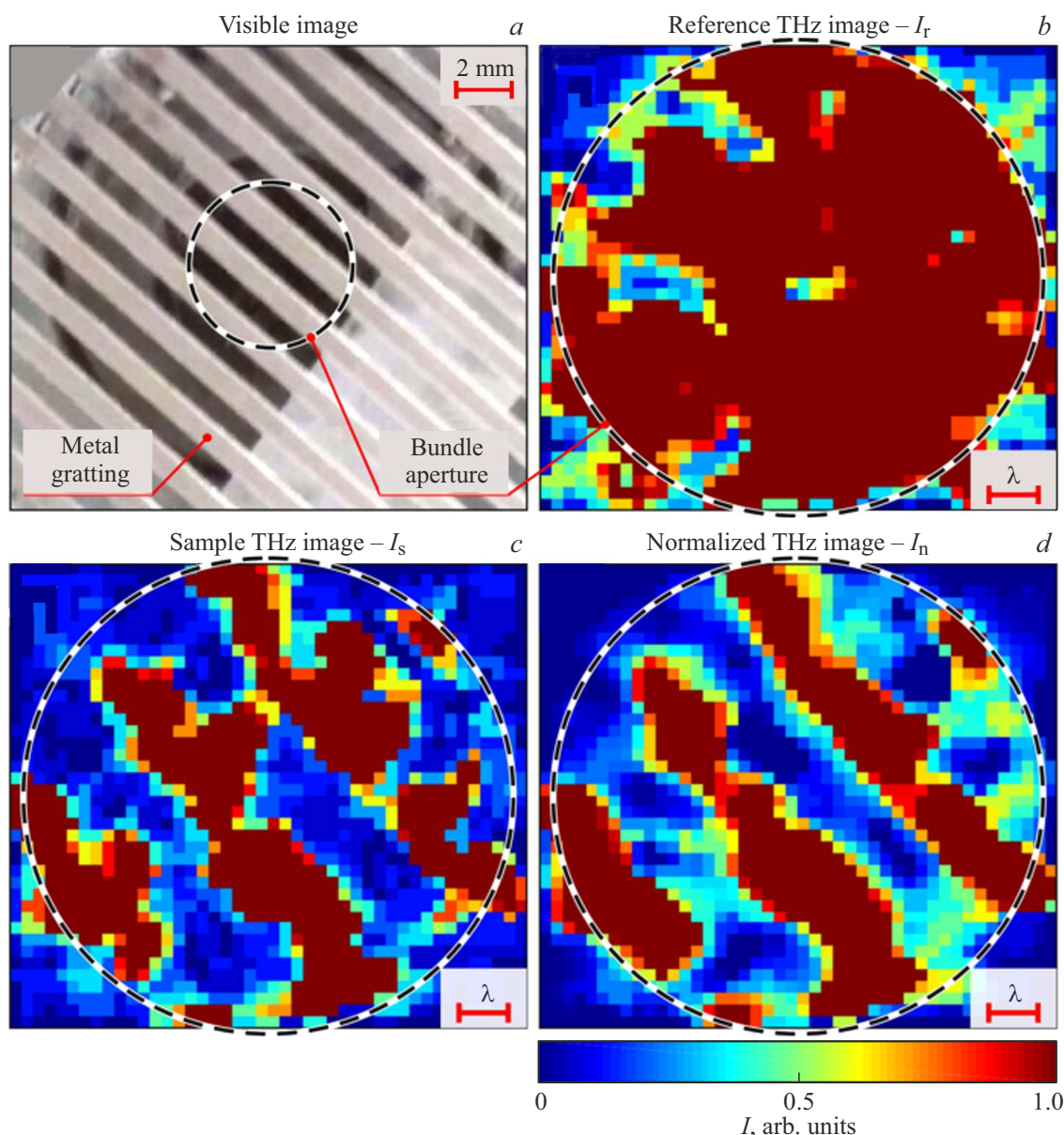


Figure 6. THz imaging of a metal grating using sapphire fiber bundle at a wavelength of $\lambda = 600 \mu\text{m}$. (a) Photo of the metal grating placed at the input end of the fiber bundle and featuring a period of 2 mm and a slit size of 1 mm. (b) Reference THz image $I_{\text{ref}}(\mathbf{r})$ formed at the output facet of the bundle without any object at the input facet. (c) Raw THz image $I_{\text{raw}}(\mathbf{r})$ formed at the output facet of the bundle with a metal grating at the input facet. (d) Normalized THz image $I_n(\mathbf{r})$ of the metal grating calculated using (8). The figure is adapted from [25] with permission from Wiley publishing house.

imaging applications, there is also considerable potential for improving its performance. An increase in the resolution of the bundle and an improvement in image quality can be achieved by increasing the thickness and conductivity of the metal coating of individual fibers, reducing fluctuations in fiber diameters over the aperture and length of the bundle, increasing the density and packing order of fibers in the bundle, and also by improving the optical quality of the bundle facets. With these improvements it will be possible to achieve resolution as low as $0.2\text{--}0.25\lambda$ and the propagation losses down to $2\text{--}4 \text{ dB cm}^{-1}$, compared

to the experimentally demonstrated $\delta = 0.3\text{--}0.5\lambda$ and $\alpha \approx 10 \text{ dB cm}^{-1}$.

3. Tapered bundle of sapphire fibers in a dielectric matrix

In this section, we present the results of studying the properties of a cone-shaped fiber bundle consisting of a tapered array of optical sapphire fibers and its use for THz-imaging with a spatial resolution exceeding the Abbe limit.

The schematic diagram for imaging using such a fiber is shown in Fig. 7, *a*, and the cross-section of the bundle along the optical axis is shown in Fig. 7, *b*. Fibers with a diameter of $300\mu\text{m}$ are arranged in an array of 21×21 (a simple square lattice) and fixed with epoxy resin in a dielectric matrix printed by a 3D-printer. Thus, each fiber is a separate pixel. Using numerical simulation, it is shown that the developed bundle is characterized by a minimum resolution at a frequency of 0.33 THz; at this frequency, the effect of energy exchange between neighbor fibers will be minimal. The fibers themselves are arranged with their input ends almost skin-to-skin and form a square 2D lattice in the object plane with a period of $p = 0.35\text{ mm}$; the common side of the square is $P = 7.0\text{ mm}$. Then the fibers diverge, maintaining the square lattice arrangement, symmetrically in the cross-section of the bundle. The bundle thickness is 11.25 mm, and the fiber lattice period in the image plane is 3 times greater than that in the object plane. This leads to stretching of the near field with a factor of $K = 3$, which makes it possible to readout the field from the output facet of the bundle with a conventional diffraction-limited lens.

3.1. Schematic of the tapered bundle of sapphire fibers and maximum spatial resolution estimate

For a comprehensive analysis of the spatial resolution of a tapered bundle, both the transmitting properties of an individual fiber and the effects of crosstalk between fibers in an array of tapered fibers must be considered.

First, the transmitting properties are numerically studied of a sapphire fiber (c KF axis directed along the optical fiber axis) fixed in epoxy resin, which simultaneously serves as a sheath with the c axis of sapphire directed along the symmetry axis of the fiber. Taking the THz optical properties of sapphire from [53] (including material anisotropy, dispersion and absorption) and epoxy properties from [41], the guiding properties of a fiber with a diameter of $300\mu\text{m}$ are analyzed using the finite-difference eigenmode (FDE) method in the ANSYS Mode software. Fig. 8, *a* shows the calculated effective refractive index n_{eff} and propagation loss α (by power) for several lowest-order guiding modes of a sapphire fiber.

It follows from the figure that our fiber operates in an effectively two-mode operation mode because only the two lowest-order modes HE_{11} and TE_{01} have losses α low enough to pass through a bundle with a length of about 1 cm. Even for these modes, losses increase significantly at lower frequencies ($\leq 0.25\text{ THz}$) due to the weak confinement in the core and high-loss overlap of the strong field with the sheath. In the same way the modal losses increase significantly at higher frequencies ($\geq 0.5\text{ THz}$) due to the increased absorption of THz waves by the sapphire. Thus, the spectral range of THz radiation input in an epoxy-coated sapphire fiber is limited by the range of 0.25–0.5 THz. Although the HE_{11} and TE_{01} modes

have very different intensity distributions in the fiber core (Fig. 8, *b*), they can be excited in a tapered bundle due to the breaking of symmetry in such structures. It is worth to note that for a bundle of parallel-laid fibers with a dielectric sheath, only the fundamental mode HE_{11} will be excited in the fiber itself, which means that the effect of intermode interference will not manifest in it.

In the absence of energy exchange between fibers, the resolution parameter δ can be determined analytically as a function of the fiber diameter d and the electromagnetic wave length in free space λ or frequency ν :

$$\delta = \frac{d}{\lambda} = \frac{d\nu}{c_0}. \quad (14)$$

As shown by the blue line in Fig. 8, *c*, for a fixed diameter of a single fiber d , this resolution parameter δ increases linearly with frequency ν . At frequencies of $\nu < 0.48\text{ THz}$, the analytical resolution exceeds the Abbe limit for free space $\delta = 0.5$. In order to estimate the effect of energy exchange between neighbor fibers on δ , the transmission of radiation through a 9×9 lattice of tapered fibers with a geometry similar to that shown in Fig. 7 is numerically simulated in the range of 0.2–0.5 THz using the finite element frequency domain (FEFD) method in the COMSOL Multyphysics software. The results of these simulations are summarized in Fig. 8, *c–e*. By the excitation of only the central pixel on the input facet of the bundle (the remaining fibers are covered by an opaque screen), the frequency-dependent point spread function (PSF) is estimated of such a model bundle (Fig. 8, *e*), which is a 1D cross section of the intensity passing through the maximum. Then the numerical resolution parameter δ at different frequencies ν is calculated by fitting this PSF with a Gaussian function and then estimating its half-width (Fig. 8, *c*). The resolution δ calculated in this way is shown by green circles in Fig. 8, *c*. It has a strong frequency-dependent behavior due to interfiber radiation exchanges (there is a significant broadening of the intensity peak, because side maxima appear in neighbor fibers). Numerical simulation makes it possible to distinguish the following spectral modes of operation of a tapered bundle:

(a) *opacity* — at low frequencies of $\nu \leq 0.24\text{ THz}$ the bundle is opaque;

(b) *strong crosstalk* — at $\nu \in (0.24, 0.3)\text{ THz}$ the resolution δ is limited by the Abbe limit due to energy exchange between fibers;

(c) *superresolution* — at $\nu \in (0.3, 0.48)\text{ THz}$, the energy exchange between fibers can be largely neglected, and the resolution δ exceeds the Abbe limit;

(d) *ordinary* — at $\nu \geq 0.48\text{ THz}$ the bundle can still be used for imaging, but it loses its superresolution capabilities.

Our numerical simulation predicts the smallest value of the resolution parameter $\delta \cong 0.35$ at a frequency of $\nu \cong 0.33\text{ THz}$. Therefore, this specific frequency was chosen for further experimental study of the tapered bundle resolution.

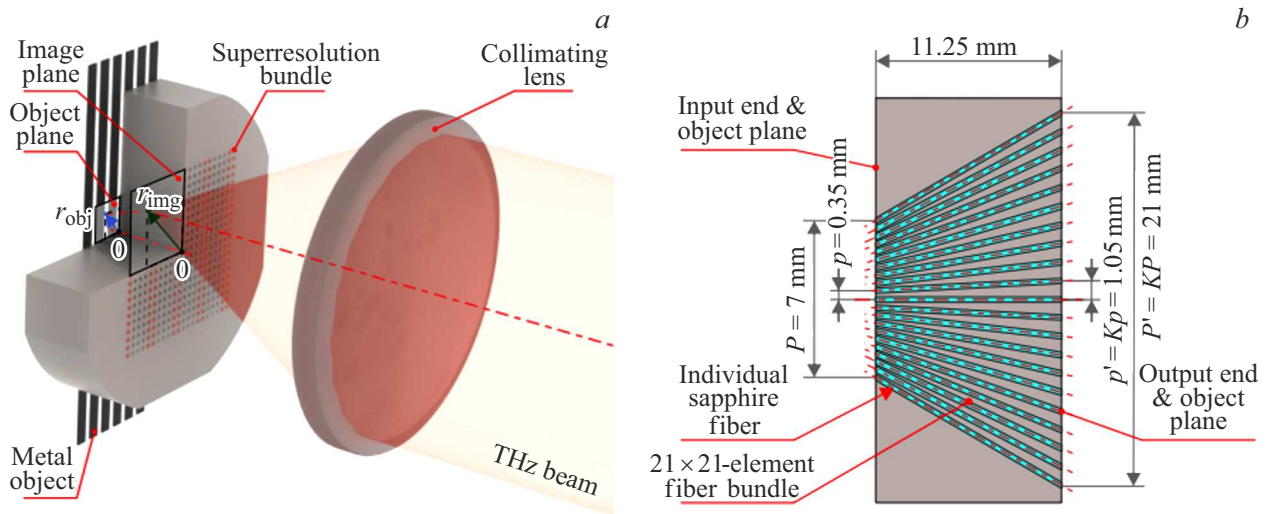


Figure 7. Tapered bundle of sapphire fibers. (a) Schematic for near-field imaging when using a tapered fiber bundle, the image is read from the output side of the bundle by a diffraction-limited optical element. (b) Cross section of the bundle along the optical axis. The figure is adapted from [36] with permission from American Physical Society publishing house.

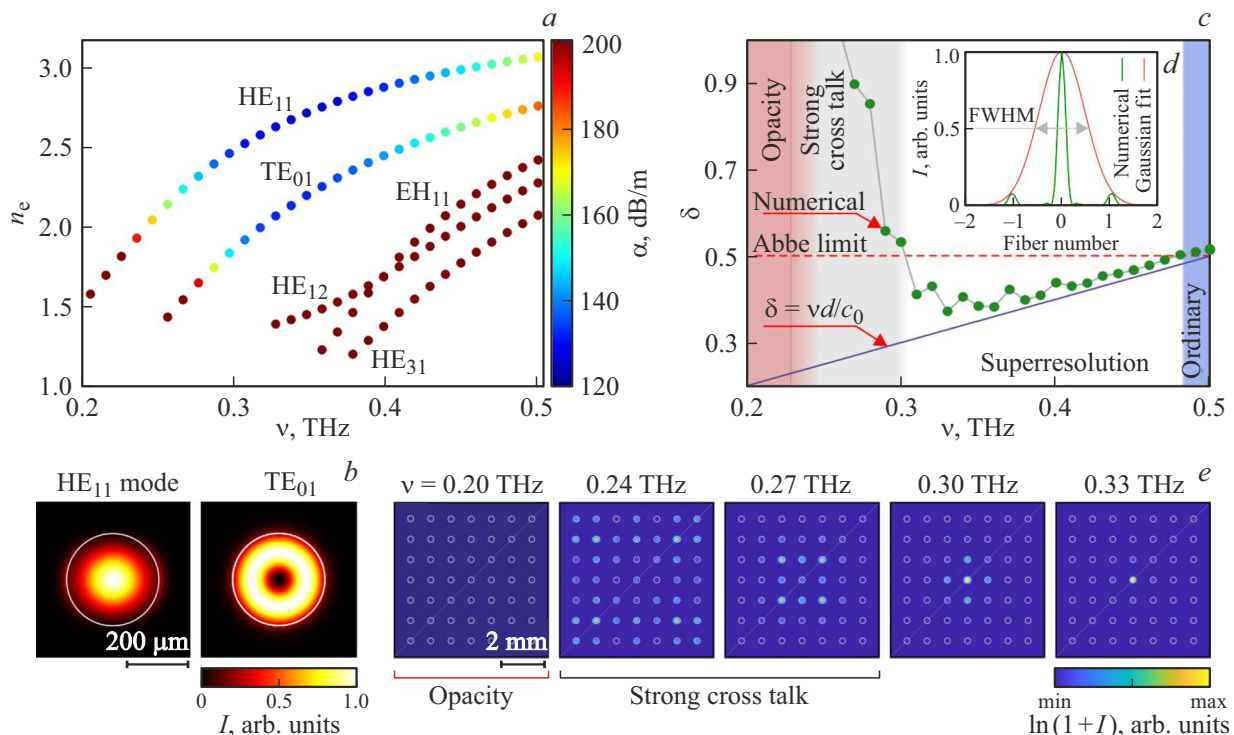


Figure 8. Numerical simulation of radiation propagation in a tapered fiber bundle. (a) Effective refractive index n_{eff} and propagation loss α (by power) of several modes in a single sapphire fiber with a diameter of $300\mu\text{m}$, with a sheath of epoxy resin. (b) Intensity distributions $I \propto E^2$ of two modes I and II with the lowest losses at a frequency of 0.33 THz . (c) Theoretical and numerical estimates of the parameter δ . (d) PSF-estimate of the bundle taking into account the effect of energy exchange between neighbor fibers in the bundle. (e) Field strength at the output facet of the output bundle obtained by numerical simulation, when the radiation is injected at the input facet only into a single central fiber. In Fig. (c), different operating modes of the tapered bundle are indicated as „opacity“, „strong crosstalk“, „superresolution“, and „ordinary“. The figure is adapted from [36] with permission from American Physical Society publishing house.

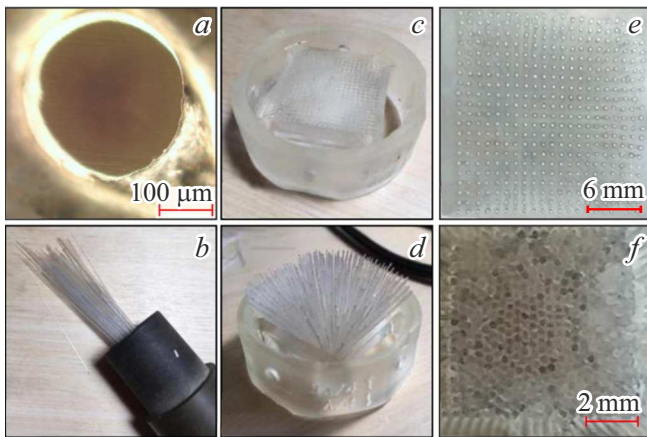


Figure 9. Stages of fabrication of the tapered fiber bundle. (a) Microscopy of an individual core with a diameter of $300\ \mu\text{m}$ of an EFG-grown sapphire fiber, being processed in the free space. (b) Photo of monodisperse ($d = 300 \pm 20\ \mu\text{m}$) sapphire fibers prepared for the bundle, assembly. (c, d) 3D printed polymer mold before and after sapphire fibers are inserted, respectively. (e, f) Microscopy of the output and input ends of a cone-shaped bundle, respectively. The figure is adapted from [36] with permission from American Physical Society publishing house.

3.2. Fabrication of the tapered fiber bundle

Sapphire fibers are produced using the EFG method of growing molded crystals directly from the Al_2O_3 melt [34,35,41], which is described in detail in [45] and in section 2; the grown fibers are then cut into pieces with a length of 2 cm, and only fibers with a diameter of d in the range of $300 \pm 20\ \mu\text{m}$ are left. Fig. 9, a, b shows a microscopy of the end facet of a typical sapphire fiber and a photo of a set of fibers used in the assembly of a fiber bundle.

As shown in Fig. 9, c, d, an array of tapered fibers is assembled using a porous polymer matrix fabricated using three-dimensional (3D) printing (Anycub LCD Photon printer with a width and depth resolution of 47 and $30\ \mu\text{m}$, respectively). The matrix has a number of holes with a diameter of $400\text{--}500\ \mu\text{m}$, into which sapphire fibers are inserted. Then the fiber matrix is immersed in epoxy resin and cured. Then the input and output ends of the bundle are ground and polished (Fig. 9, e, f). As a result, on the output facet of the bundle (image plane), the fibers form an almost perfect square array (Fig. 9, e), while on the input facet (object plane), the fiber array is somewhat disordered, which is caused by a slight displacement of the fibers during the process of curing of the epoxy resin (Fig. 9, f).

3.3. Experimental imaging using a sapphire fiber bundle

With the use of the original imaging system described in Section 2.3.3, images were obtained at a frequency of 0.33 THz using the fabricated bundle. In the experimental

setup, the displayed object is located in immediate contact with the input facet of the bundle and is illuminated by a slightly focused spatially homogeneous THz-beam.

The illumination of a partially opaque object forms a spatial distribution of the field strength in the object plane $I_{\text{obj}}(\mathbf{r}_{\text{obj}})$, where \mathbf{r}_{obj} is a vector in the object plane. Then the THz field is injected into the fiber bundle, directed to the output facet of the bundle, and stretched with a magnification factor of $K \simeq 3$ by the tapered fiber lattice. On the output facet of the bundle, the THz field strength distribution $I_{\text{img}}(\mathbf{r}_{\text{img}})$ is formed, where \mathbf{r}_{img} is the vector in the image plane, which, in the absence of energy exchanges between fibers and intermodal interference, is associated with the intensity distribution in the object plane as follows:

$$I_{\text{img}}(\mathbf{r}_{\text{img}}) = I_{\text{obj}}\left(\frac{\mathbf{r}_{\text{img}}}{K}\right). \quad (15)$$

The intensity distribution $I_{\text{img}}(\mathbf{r}_{\text{img}})$ is then read from the output facet of the bundle from a wide-aperture lens acting as a diffraction-limited lens. This system used a motorized 2D raster scanner equipped with a wide-aperture diffraction-limited lens and a Golay cell. The lens collimates the THz radiation from the diffraction-limited region of the output facet of the bundle (a diaphragm with a diameter of λ is used to reduce noise) and directs it to the detector.

A. Image processing

Fig. 10, a, b shows a photo of a test object, which is a lattice of metal strips with a period of 1.8 mm and a metal strip width of 0.9 mm, as well as its THz-image obtained through a tapered fiber bundle at $\nu = 0.33\ \text{THz}$ ($\lambda = 917\ \mu\text{m}$). Although several periods of the metal lattice are clearly visible even in the raw THz-image (Fig. 10, b), it needs to be further improved to mitigate the various measurement artifacts that are typical for imaging with such fiber bundles; among them, worth-noting are the image pixelization (a THz-image looks like a set of individual speckles), image intensity fluctuations (transmission of individual fibers changes over the bundle aperture due to changes in their optical properties), noises like „salt and pepper“ (some pixels may be defective or, conversely, provide a much higher transmission than average).

To mitigate these difficulties, the resulting image is digitally processed. First, the pixelization is suppressed using a quadratic moving average (smoothing) filter $f(\mathbf{r}_{\text{img}})$ on the output facet of the bundle with a width and a height equal to the period of the fiber lattice:

$$I_{\text{filt}}(\mathbf{r}_{\text{img}}) = I_{\text{img}}(\mathbf{r}_{\text{img}}) \circledast f(\mathbf{r}_{\text{img}}). \quad (16)$$

Second, the THz-image is scaled with an inverse magnification factor K^{-1} to restore it in the object plane, followed by resampling. Finally, the inverse filtering is used to correct inhomogeneities in the image intensity. To this end, we obtain a reference image $I_{\text{img}}^{\text{ref}}(\mathbf{r})$ on the output facet of the bundle in the absence of an imaged object,

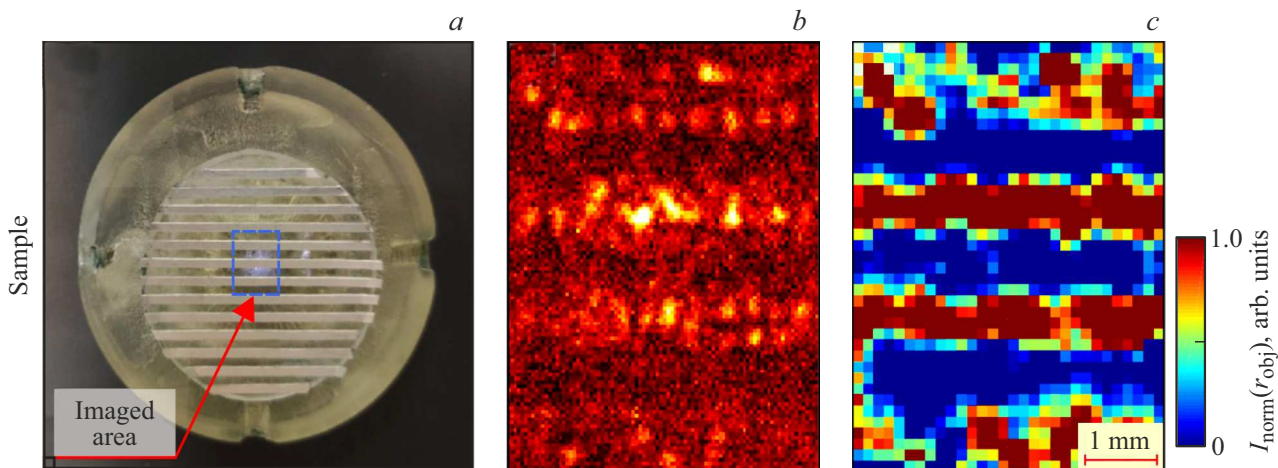


Figure 10. Processing of THz-images obtained using a tapered fiber bundle at a frequency of $\nu = 0.33$ THz ($\lambda \simeq 917 \mu\text{m}$). (a) Phot of the input facet of the bundle in contact with the test object. (b) Measured $I_{\text{img}}(\mathbf{r}_{\text{img}})$. (c) Normalized image in the THz range, $I_{\text{norm}}(\mathbf{r}_{\text{obj}})$, obtained using equation (17). The figure is adapted from [36] with permission from American Physical Society publishing house.

and then apply smoothing and resampling using the same parameters as for the THz-image of the sample. Then the image of the object is normalized to the reference image using the regularization procedure described in [36]. The reconstructed in this way THz-image in the object plane $I_{\text{norm}}(\mathbf{r}_{\text{obj}})$ is shown in Fig. 10, c, while the effects of image pixelization, intensity inhomogeneities, and damaged pixels are effectively softened by image processing.

B. Resolution estimate

To experimentally estimate the spatial resolution of a tapered fiber bundle, a standard technique is used, which consists in imaging of test objects with sharp changes in their transmission (detailed description is given in [25,36], as well as in Section 2.3.3). Particularly, a strip of metal foil with a straight edge is used as an object. Due to the fact that fibers in the bundle are packed in a square lattice, the resolution can be studied in several directions (horizontal, vertical and diagonal, as shown in Fig. 11, a–e). To estimate the resolution, the first derivative of the image intensity profile $dl_{\text{norm}}(\mathbf{r})/d\mathbf{r}$ is calculated in the \mathbf{r} direction perpendicular to the imaged edge of the metal foil. Due to the fact that the $dl_{\text{norm}}(\mathbf{r})/d\mathbf{r}$ function can be considered as a PSF-approximation of the imaging system [58], the resolution parameter δ is calculated at each point along the edge of the metal foil as the half-width of the central peak of the function, normalized to $\lambda = 917 \mu\text{m}$. By studying various positions and orientations of the foil edge on the input facet of the bundle, the statistics of the spatial distribution of the resolution parameter δ is collected, which is then approximated by the Gaussian function (Fig. 11, g). As expected, the resolution thus characterized differs for the perpendicular and diagonal directions with mean values of $\langle \delta \rangle = 0.347$ and 0.543 and standard deviations of $\sigma_{\text{delta}} = 0.148$ and 0.171 , respectively.

The observed change in resolution on the input facet of the bundle can be explained if we consider a disordered lattice formed by fibers in the object plane. In particular, Fig. 11, h shows a photo of the input facet of the bundle, and Fig. 11, i, j shows Voronoi cells and the pair correlation function $g(\mathbf{r})$ (calculated for the corresponding partially disordered lattice formed by sapphire fibers (nodes) [25]. Edge nodes (fibers) have fewer nearest neighbors, making the data more difficult to read. Therefore, for convenience, in the panel of Fig. 11, i we do not show cells for edge nodes. It can be seen on the (i) graph, that most of the nodes have six nearest neighbors, and this number fluctuates somewhat along the bundle aperture. If for an ideal crystal lattice clearly distinguished peaks at $g(\mathbf{r})$ are δ -Dirac functions, then for a somewhat disordered lattice such peaks are broadened. Among them, the first and the second peaks stand out, because they determine the statistics of the distances between a lattice node and its nearest neighbors in the vertical or horizontal and diagonal directions, respectively. By approximating the peaks $g(\mathbf{r})$ by the Gaussian function, the statistical data for the nearest neighbor separation (Fig. 11, j) turn out to be very close to the results of direct experimental measurements of the resolution (Fig. 11, g). In particular, the average values of $\langle \delta \rangle = 0.373$ and 0.515 for the first and second peaks almost completely agree with our experimental estimates, which confirms that fiber lattice disorder is the main factor responsible for the change in the resolution over the bundle aperture.

4. Conclusions

This review covers two types of bundles of high-refractive-index optical fibers for imaging with a spatial resolution exceeding the diffraction limit. The first type of bundles is an array of sapphire fibers laid in parallel, where fibers can

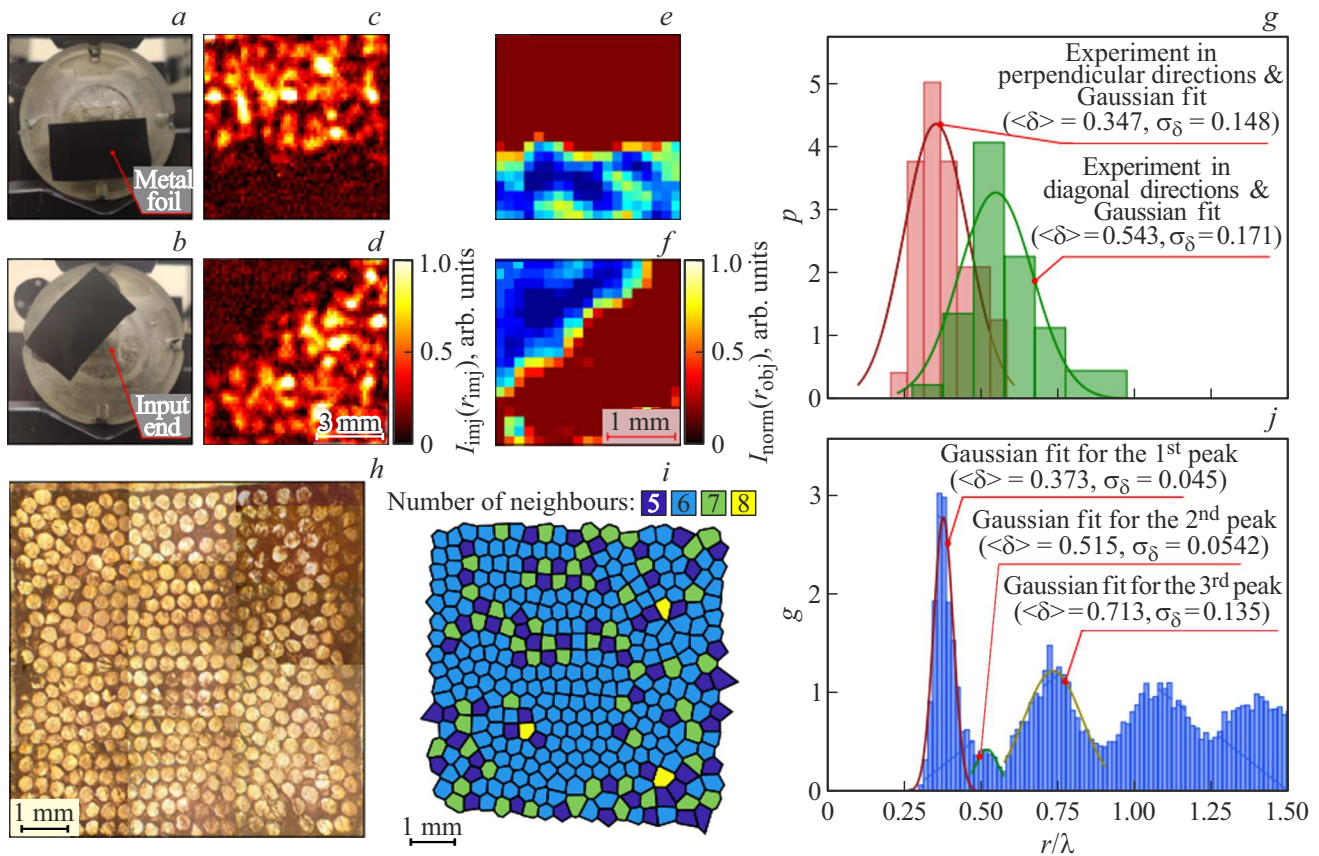


Figure 11. Spatial resolution of a tapered fiber bundle at a frequency of $\nu = 0.33$ THz ($\lambda \approx 917 \mu\text{m}$). (a, b) Photos of a metal strip with a straight edge used as test objects oriented horizontally, vertically, or diagonally. (c, d) Measured $I_{\text{img}}(\mathbf{r}_{\text{img}})$ and (e, f) normalized $I_{\text{norm}}(\mathbf{r}_{\text{obj}})$ THz-images of this test object with different orientations. (g) Statistics of the change in the resolution parameter δ over the bundle aperture in the perpendicular and diagonal directions relative to the bundle's square lattice, caused by lattice disorder and approximated by a Gaussian distribution. (h) Microscopy of the input facet of the bundle. (i) Representation of the input facet of the bundle using Voronoi cells, colored according to the number of nearest neighbors of each fiber (node). (g) Pair correlation function $g(\mathbf{r})$ for a partially disordered fiber lattice along with a Gaussian approximation for its first, second and third peaks. The figure is adapted from [36] with permission from American Physical Society publishing house.

be either metal-coated or dielectric-coated. The first type of such bundle consists of parallel-laid sapphire fibers with a diameter of $300 \mu\text{m}$ and a bundle period of 0.45 mm , and the other type, investigated in this study, consists of optical sapphire fibers with a diameter of $300 \mu\text{m}$ with a metal coating and a length of 20 mm , parallel-laid close to each other and forming a hexagonal lattice.

It has been experimentally and theoretically demonstrated that a THz imaging system based on a bundle of metal-coated fibers is characterized by subwavelength spatial resolution. The analysis of the pair correlation function of the fiber lattice, as well as direct measurements of the spatial resolution by the „sharp-blade“ method and THz imaging of an opaque metal corner made it possible to determine the resolution of the bundle in a series of independent measurements. Due to some disorder of the fiber lattice, the resolution of the bundle will change along its aperture and will be $\langle \delta \rangle = 0.53 \pm 0.15 \lambda$, where $\lambda = 600 \mu\text{m}$, and the smallest resolution reached $\delta = 0.3$ in some areas of the bundle. Thus, it is confirmed that the sapphire fiber

bundle has a resolution close to the Abbe diffraction limit and demonstrates significant potential for subwavelength imaging.

The second type of bundles is a cone-shaped bundle composed of a tapered array of sapphire optical fibers with a fiber diameter of $300 \pm 20 \mu\text{m}$ and an optical quality of the surface. Such a bundle allows transmitting a near THz field with an inhomogeneity scale smaller than the diffraction limit, and then scales the intensity distribution by several times, which makes it possible to read the recorded field using a diffraction-limited element. The bundle period in the object area is 0.35 mm and that in the image plane is 1.05 mm . Numerical calculations have shown that at frequencies of $\nu < 0.48$ THz the spatial resolution exceeds the Abbe limit.

The resolution of such a bundle of tapered sapphire fibers with a high refractive index was measured. The measured resolution was $\langle \delta \rangle = 0.34 \pm 0.15 \lambda$, which is in good agreement with the numerically predicted value of $\delta = 0.35 \lambda$ at an operating wavelength of $\lambda = 917 \mu\text{m}$.

These results demonstrate the significant potential for ultra-high resolution imaging with such taper fiber bundles. It also provides a convenient and energy efficient reading of the field distribution using standard optical diffraction-limited elements. In addition, it can be concluded that the use of metal-coated fiber bundles is more promising for high frequencies (about $\nu \approx 0.5$ and higher), and dielectric-coated fibers will be more efficient at low frequencies, although the resolution will be affected by the crosstalk effect between fibers.

Thus, this review provides information on new THz imaging methods based on the use of bundles of sapphire optical fibers, which make it possible to overcome the Abbe diffraction limit. Optical fiber bundles based on high-refractive-index sapphire fibers can be useful in biophotonics for ultra-high resolution imaging exceeding the Abbe diffraction limit for the free space. This means that such bundles can provide more accurate and detailed imaging of objects in biological tissues and organs. In addition, methods for restoring THz-images of test binary objects obtained using the proposed bundles can be used to diagnose various diseases and pathologies in medical practice.

Conflict of interest

The authors declare that they have no conflict of interest.

References

- [1] G. Agrawal. *Nonlinear Fiber Optics*, 4th ed. (Elsevier Science, USA, 2007).
- [2] G. Keiser, F. Xiong, Y. Cui, P. Shum. *J. Biomed. Opt.*, **19**, 080902 (2014). DOI: 10.1117/1.jbo.19.8.080902
- [3] J. Li, H. Ebdorff-Heidepriem, B. Gibson, A. Greentree, M. Hutchinson, P. Jia, R. Kostecki, G. Liu, A. Orth, M. Ploschner, E. Schartner, S. Warren-Smith, K. Zhang, G. Tsiminis, E. Goldys. *APL Photonics*, **3**, 100902 (2018). DOI: 10.1063/1.5040861
- [4] C. Lee, C. Engelbrecht, T. Soper, F. Helmchen, E. Seibel. *J. Biophotonics*, **3** (5–6), 385 (2010). DOI: 10.1002/jbio.200900087
- [5] L. Doronina-Amitonova, I. Fedotov, O. Efimova, M. Chernysheva, A. Fedotov, K. Anokhin, A. Zheltikov. *Appl. Phys. Lett.*, **101**, 233702 (2012). DOI: 10.1063/1.4864646
- [6] S. Sivankutty, A. Bertocini, V. Tsvirkun, N.G. Kumar, G. Brévalle, G. Bouwmans, E.R. Andresen, C. Liberale, H. Rigneault. *Opt. Lett.*, **46** (19), 4968 (2021). DOI: 10.1364/OL.435063
- [7] Y. Lavi, A. Millo, A. Katzir. *Appl. Phys. Lett.*, **87**, 241122 (2005). DOI: 10.1063/1.2141728
- [8] W. Xing, L. Wang, K. Maslov, L. Wang. *Opt. Lett.*, **38** (1), 52 (2013). DOI: 10.1364/OL.38.000052
- [9] B. Flusberg, E. Cocker, W. Piyawattanametha, J. Jung, E. Cheung, M. Schnitzer. *Nat. Methods*, **2**, 941 (2005). DOI: 10.1038/nmeth820
- [10] W. Gobel, J. Kerr, A. Nimmerjahn, F. Helmchen. *Opt. Lett.*, **29** (21), 2521 (2004). DOI: 10.1364/OL.29.002521
- [11] L. Doronina-Amitonova, I. Fedotov, A. Fedotov, A. Zheltikov. *Appl. Phys. Lett.*, **102**, 161113 (2013). DOI: 10.1063/1.4801847
- [12] B. Lee, S. Han, Y. Jeong, J. Paek. *Opt. Lett.*, **29** (1), 116 (2004). DOI: 10.1364/OL.29.000116
- [13] T. Xie, D. Mukai, S. Guo, M. Brenner, Z. Chen. *Opt. Lett.*, **30** (14), 1803 (2005). DOI: 10.1364/OL.30.001803
- [14] M. Pochechuev, I. Fedotov, A. Zheltikov. *Appl. Phys. Lett.*, **113**, 191102 (2018). DOI: 10.1063/1.5054316
- [15] A. Orth, M. Ploschner, E. Wilson, I. Maksymov, B. Gibson. *Sci. Adv.*, **5** (4), eaav1555 (2019). DOI: 10.1126/sciadv.aav1555
- [16] R.P.J. Barretto, T.H. Ko, J.C. Jung, T.J. Wang, G. Capps, A.C. Waters, Y. Ziv, A. Attardo, L. Recht, M.J. Schnitzer. *Nat. Med.*, **17**, 223 (2011). DOI: 10.1038/nm.2292
- [17] V. Szabo, C. Ventalon, V. DeSars, J. Bradley, V. Emiliani. *Neuro Resource*, **84** (6), 1157 (2014). DOI: 10.1016/j.neuron.2014.11.005
- [18] A. Yetisen, H. Qu, A. Manbachi, H. Butt, M. Dokmeci, J. Hinstroza, M. Skorobogatiy, A. Khademhosseini, S. Yun. *ACS Nano*, **10** (3), 3042 (2016). DOI: 10.1021/acsnano.5b08176
- [19] P. Gutruf, C. Good, J. Rogers. *APL Photonics*, **3**, 120901 (2018). DOI: 10.1063/1.5040256
- [20] D. Kim, J. Moon, M. Kim, T. Yang, J. Kim, E. Chung, W. Choi. *Opt. Lett.*, **39** (7), 1921 (2014). DOI: 10.1364/OL.39.001921
- [21] J.-H. Han, S. Yoon. *Opt. Lett.*, **36** (16), 3212 (2011). DOI: 10.1364/OL.36.003212
- [22] J. Shao, W.-C. Liao, R. Liang, K. Barnard. *Opt. Lett.*, **43** (8), 1906 (2018). DOI: 10.1364/OL.43.001906
- [23] J. Shao, J. Zhang, X. Huang, R. Liang, K. Barnard. *Opt. Lett.*, **44** (5), 1080 (2019). DOI: 10.1364/OL.44.001080
- [24] A. Porat, E.R. Andresen, H. Rigneault, D. Oron, S. Gigan, O. Katz. *Opt. Express*, **24** (15), 16835 (2016). DOI: 10.1364/OE.24.016835
- [25] K. Zaytsev, G. Katyba, N. Chernomyrdin, I. Dolganova, A. Kucheryavenko, A. Rossolenko, V. Tuchin, V. Kurlov, M. Skorobogatiy. *Adv. Opt. Mater.*, **8** (18), 2000307 (2020). DOI: 10.1002/adom.202000307
- [26] R. Stantchev, B. Sun, S. Hornett, P. Hobson, G. Gibson, M. Padgett, E. Hendry. *Sci. Adv.*, **2**, e1600190 (2016). DOI: 10.1126/sciadv.1600190
- [27] Y. Choi, C. Yoon, M. Kim, T.D. Yang, C. Fang-Yen, R. Dasari, K. Lee, W. Choi. *Phys. Rev. Lett.*, **109**, 203901 (2012). DOI: 10.1103/PhysRevLett.109.203901
- [28] P. Belov, C. Simovski, P. Ikonen. *Phys. Rev. B*, **71**, 193105 (2005). DOI: 10.1103/PhysRevB.71.193105
- [29] P. Belov, Y. Zhao, S. Sudhakaran, A. Alomainy, Y. Hao. *Appl. Phys. Lett.*, **89**, 262109 (2006). DOI: 10.1063/1.2424557
- [30] K. Kaltenecker, A. Tuniz, S. Fleming, A. Argyros, B. Kuhlmeier, M. Walther, B. Fischer. *Optica*, **3** (5), 458 (2016). DOI: 10.1364/OPTICA.3.000458
- [31] A. Tuniz, B. Kuhlmeier, R. Lwin, A. Wang, J. Anthony, R. Leonhardt, S. Fleming. *Appl. Phys. Lett.*, **96**, 191101 (2010). DOI: 10.1063/1.3428576
- [32] M. Habib, A. Stefani, S. Atakaramians, S. Fleming, A. Argyros, B. Kuhlmeier. *Appl. Phys. Lett.*, **110**, 101106 (2017). DOI: 10.1063/1.4978445
- [33] D.W. Vogt, J. Anthony, R. Leonhardt. *Opt. Exp.*, **23** (26), 33359 (2015). DOI: 10.1364/OE.23.033359
- [34] G. Katyba, K. Zaytsev, I. Dolganova, I. Shikunova, N. Chernomyrdin, S. Yurchenko, G. Komandin, I. Reshetov, V. Nesvizhevsky, V. Kurlov. *Prog. Cryst. Growth Charact. Mater.*, **64** (4), 133 (2018). DOI: 10.1016/j.pcrysgrow.2018.10.002
- [35] G. Katyba, K. Zaytsev, I. Dolganova, N. Chernomyrdin, V. Ulitko, S. Rossolenko, I. Shikunova, V. Kurlov. *Prog.*

- Cryst. Growth Charact. Mater., **67** (3), 100523 (2021). DOI: 10.1016/j.pcrysgrow.2021.100523
- [36] G.M. Katyba, M. Skorobogatiy, D.G. Melikyants, N.V. Chernomyrdin, A.N. Perov, E.V. Yakovlev, I.N. Dolganova, I.E. Spektor, V.V. Tuchin, V.N. Kurlov, K.I. Zaytsev. Phys. Rev. Appl., **18**, 034069 (2022). DOI: 10.1103/PhysRevApplied.18.034069
- [37] D. Grischkowsky, S. Keiding, M. van Exter, Ch. Fattinger. J. Opt. Soc. Am. B, **7** (10), 2006 (1990). DOI: 10.1364/JOSAB.7.002006
- [38] H. Chen, M. Buric, P. Ohodnicki, J. Nakano, B. Liu, B. Chorpening. Appl. Phys. Rev., **5**, 011102 (2018). DOI: 10.1063/1.5010184
- [39] I. Minin, O. Minin, G. Katyba, N. Chernomyrdin, V. Kurlov, K. Zaytsev, L. Yue, Z. Wang, D. Christodoulides. Appl. Phys. Lett., **114**, 031105 (2019). DOI: 10.1063/1.5065899
- [40] P. Martin. Phys. Rev., **161**, 143 (1967). DOI: 10.1103/PhysRev.161.143
- [41] G.M. Katyba, D.G. Melikyants, N.V. Chernomyrdin, V.N. Kurlov, K.I. Zaytsev. Opt. Engineering, **60** (8), 082010 (2021). DOI: 10.1117/1.OE.60.8.082010. (03)90001-5
- [42] N.V. Chernomyrdin, G.M. Katyba, A.A. Gavdush, T.V. Frolov, I.N. Dolganova, V.N. Kurlov, K.I. Zaytsev. Proc. SPIE, **11088**, 110880I (2019). DOI: 10.1117/12.2528741
- [43] N.V. Abrosimov, V.N. Kurlov, S.N. Rossolenko. Prog. Cryst. Growth Charact. Mater., **46** (1–2), 1 (2003). DOI: 10.1016/S0960-8974(03)90001-5
- [44] P.I. Antonov, V.N. Kurlov. Prog. Cryst. Growth Charact. Mater., **44** (2), 63 (2002). DOI: 10.1016/S0960-8974(02)00005-0
- [45] G. Katyba, K. Zaytsev, N. Chernomyrdin, I. Shikunova, G. Komandin, V. Anzin, S. Lebedev, I. Spektor, V. Karasik, S. Yurchenko, I. Reshetov, V. Kurlov, M. Skorobogatiy. Adv. Opt. Mater., **6** (22), 1800573 (2018). DOI: 10.1002/adom.201800573
- [46] K.I. Zaytsev, G.M. Katyba, V.N. Kurlov, I.A. Shikunova, V.E. Karasik, S.O. Yurchenko. IEEE Trans. Terahertz Sci. Technol., **6** (4), 576 (2016). DOI: 10.1109/TTHZ.2016.2555981
- [47] G.M. Katyba, N.V. Chernomyrdin, I.N. Dolganova, A.A. Proinin, I.V. Minin, O.V. Minin, K.I. Zaytsev, V.N. Kurlov. Proc. SPIE, **11164**, 111640G (2019). DOI: 10.1117/12.2536305
- [48] E. Yakovlev, K. Zaytsev, I. Dolganova, S. Yurchenko. IEEE Trans. Terahertz Sci. Technol., **5** (5), 810 (2015). DOI: 10.1109/TTHZ.2015.2460671
- [49] Lumerical Mode Solutions. [Electronic source]. URL: <https://www.lumerical.com>
- [50] V.V. Gerasimov, B.A. Knyazev, A.K. Nikitin, G.N. Zhizhin. Appl. Phys. Lett., **98**, 171912 (2011). DOI: 10.1063/1.3584130
- [51] T.H. Isaaca, W.L. Barnes, E. Hendry. Appl. Phys. Lett., **93**, 241115 (2008). DOI: 10.1063/1.3049350
- [52] M.A. Ordal, R.J. Bell, R.W. Alexander, L.L. Long, M.R. Querry. Appl. Opt., **24** (24), 4493 (1985). DOI: 10.1364/AO.24.004493
- [53] M.S. Islam, C.M.B. Cordeiro, M.A.R. Franco, J. Sultana, A.L.S. Cruz, D. Abbott. Opt. Express, **28** (11), 16089 (2020). DOI: 10.1364/OE.389999
- [54] D.V. Lavrukhin, A.E. Yachmenev, I.A. Glinskiy, R.A. Khabibullin, Y.G. Goncharov, M. Ryzhii, T. Otsuji, I.E. Spector, M. Shur, M. Skorobogatiy, K.I. Zaytsev, D.S. Ponomarev. AIP Adv., **9**, 015112 (2019). DOI: 10.1063/1.5081119
- [55] V. Setti, L. Vincetti, A. Argyros. Opt. Express, **21** (3), 3388 (2013). DOI: 10.1364/OE.21.003388
- [56] T. Ma, A. Markov, L. Wang, M. Skorobogatiy. Opt. Express, **23** (6), 7856 (2015). DOI: 10.1364/OE.23.007856
- [57] A. Markov, M. Skorobogatiy. Appl. Phys. Lett., **103**, 181118 (2013). DOI: 10.1364/OE.21.012728
- [58] D.F. Gardner, M. Tanksalvala, E.R. Shanblatt, X. Zhang, B.R. Galloway, C.L. Porter, R. Karl Jr., C. Bevis, D.E. Adams, H.C. Kapteyn, M.M. Murnane, G.F. Mancini. Nat. Photonics, **11**, 259 (2017). DOI: 10.1364/LS.2017.LM3F4

Translated by Y.Alekseev